A Time-Frequency Distribution-Based Approach for Decoding Visually Imagined Objects Using EEG Signals

RAMI ALAZRAI[©1], **(Member, IEEE), AMAL AL-SAQQAF**[1], **FERAS AL-HAWARI**[©1],
HISHAM ALWANNI[2], **AND MOHAMMAD I. DAOUD**[©1]

[1]Department of Computer Engineering, School of Electrical Engineering and Information Technology, German Jordanian University, Amman 11180, Jordan
[2]Faculty of Engineering, University of Freiburg, 79098 Freiburg, Germany

Corresponding author: Rami Alazrai (rami.azrai@gju.edu.jo)

ABSTRACT This paper investigates the possibility of using visual imagery tasks, which are mental imagery tasks that involve imagining the images of objects perceptually without seeing them, as a control paradigm that can increase the control's dimensionality of electroencephalography (EEG)-based brain-computer interfaces. Specifically, we propose an EEG-based approach for decoding visually imagined objects by using the Choi-Williams time-frequency distribution to analyze the EEG signals in the joint time-frequency domain and extract a set of twelve time-frequency features (TFFs). The extracted TFFs are used to construct a multi-class support vector machine classifier to decode various visually imagined objects. To validate the performance of our proposed approach, we have recorded an EEG dataset for 16 healthy subjects while imagining objects that belong to four different categories, namely nature (fruits and animals), decimal digits, English alphabet (capital letters), and arrow shapes (arrows with different colors and orientations). Moreover, we have designed two performance evaluation analyses, namely the channel-based analysis and feature-based analysis, to quantify the impact of utilizing different groups of EEG electrodes that cover various regions on the scalp and the effect of reducing the dimensionality of the extracted TFFs on the performance of our proposed approach in decoding the imagined objects within each of the four categories. The experimental results demonstrate the efficacy of our proposed approach in decoding visually imagined objects. Particularly, the average decoding accuracies obtained for each of the four categories were as high as 96.67%, 93.64%, 88.95%, and 92.68%.

INDEX TERMS Visual imagery, electroencephalography (EEG), time-frequency distribution, brain-computer interface (BCI), support vector machine (SVM), pattern recognition.

I. INTRODUCTION

A brain-computer interface (BCI) is a system that analyzes the electrophysiological signals of the brain and produces commands that reflect the user's mental activities [1]–[4]. Over the past two decades, researchers have developed BCI systems for different application domains, such as assisting individuals with severe motor-impairments [1], [5]–[7], recognizing emotional states [8], and detecting pain [9]–[11]. In this regard, various types of neuroimaging modalities have been utilized to record brain activities and design BCI

The associate editor coordinating the review of this manuscript and approving it for publication was Gang Wang[©].

systems [4], such as the functional magnetic resonance imaging (fMRI), positron emission tomography (PET), electroencephalography (EEG), and electrocorticography (ECoG). Among these different neuroimaging modalities, the EEG neuroimaging modality, which records the electrical activities of the brain that are measured at the scalp [4], has been widely employed to design BCI systems in various application domains [4], [12]. This can be attributed to the following factors [2], [4], [12]: (1) the noninvasive nature of the EEG modality, (2) the high temporal resolution of the acquired EEG signals, and (3) the relatively low cost and high portability of the EEG acquisition devices compared with the acquisition devices of other neuroimaging modalities.

IEEE *Access*

R. Alazrai *et al.*: Time-Frequency Distribution-Based Approach for Decoding Visually Imagined Objects Using EEG Signals

Recent clinical studies have indicated that mental imagery tasks can be employed to design BCI systems that can facilitate the treatment of several mental disorders [13]. In this regard, the literature indicates that the motor imagery (MI) task, which refers to the process of imagining the movement of a particular body-part (e.g. the hand or the foot) without actually moving it [14], is by far the most commonly used mental task to design EEG-based BCI systems [2], [15]–[17]. In fact, the majority of the existing MI EEG-based BCI systems are focused on developing signal processing and analysis techniques to distinguish between MI tasks associated with a limited number of body-parts [18]–[25], including the right hand, left hand, right foot, left foot, and tongue. Despite the promising results attained by the existing MI EEG-based BCI systems in decoding MI tasks that are associated with different body parts, these systems are capable of producing a relatively limited control's dimensionality. The control's dimensionality of a BCI system is defined as the number of control signals that can be generated from the BCI system, where the number of these control signals is related to the number of imagery tasks considered by the BCI system. This in turn can significantly reduce the potential of utilizing these BCI systems to support real-world applications that usually require a high number of control signals [6], [7].

To increase the control's dimensions of the BCI systems, researchers have investigated the possibility of decoding other mental imagery tasks, namely the visual imagery of objects [2], [12], [26]–[29]. The visual imagery of an object is a mental process that involves regenerating and maintaining the image of the object perceptually without seeing it [30]–[32]. This mental task has been mainly investigated using two neuroimaging modalities [28], [33]–[39], namely fMRI and PET. Nonetheless, several limitations, such as the high acquisition cost, low portability, and the requirement of the subject to sit or lay down in the scanner, might restrict the use of these neuroimaging modalities to be only in clinics and research labs. To alleviate these limitations, researchers have recently started to study the possibility of using the EEG neuroimaging modality to decode visually imagined objects [2], [12], [40], [41]. However, decoding the visually imagined objects by analyzing the EEG signals is a difficult task. This is due to the inter- and intra-personal variations in the generated brain activities during the imagination of similar and different objects [42], [43]. Moreover, the EEG signals are nonstationary signals that have time-varying spectral characteristics, which implies that analyzing the EEG signals in the time-domain only or the frequency-domain only might not be sufficient. Therefore, a joint time-frequency analysis is required to capture the time-varying spectral characteristics of the EEG signals [44].

In this study, we propose an EEG-based approach for decoding a large number of visually imagined objects using a set of time-frequency features (TFFs) that are extracted from the Choi-Williams time-frequency distribution. Specifically, we utilize the Choi-Williams distribution to analyze the EEG signals in the joint time-frequency domain and capture the time-varying spectral characteristics of the EEG signals. To reduce the high dimensionality of the Choi-Williams distribution computed for the EEG signals, a set of twelve TFFs are extended from the time-domain and frequency-domain to the joint time-frequency domain and extracted from the Choi-Williams distribution computed for the EEG signals. These TFFs are used to construct a subject-specific multi-class support vector machine classifier to decode the visually imagined objects.

In order to validate the performance of our proposed approach, we have recorded a large visual imagery EEG dataset that is collected from 16 healthy subjects while imagining objects that belong to four different categories, namely nature (fruits and animals), decimal digits, English alphabet (capital letters), and arrow shapes (arrows with different colors and orientations). For each subject, the number of imagined objects, number of trials, and approximate total EEG recording time are 56 objects, 440 trials, and 2.2 hours, respectively. Moreover, we have developed two performance evaluation analyses to assess the performance of the proposed approach in decoding the visually imagined objects of each of the four categories. The first performance evaluation analysis, which we refer to as the channel-based analysis, quantifies the effect of utilizing different groups of EEG electrodes, which cover various regions of the brain, on the ability of our proposed approach to distinguish between the EEG signals associated with the visually imagined objects within each of the four categories. The second performance evaluation analysis, which we refer to as the feature-based analysis, quantifies the effect of utilizing different subsets of the extracted TFFs on the ability of our proposed approach to distinguish between the EEG signals associated with the visually imagined objects within each of the four categories. The results presented in this study illustrate the capability of the proposed approach to accurately decode the visually imagined objects within each of the four categories in our EEG dataset. In addition, the results obtained using the proposed approach outperform those reported in several existing state-of-the-art approaches in terms of the number of decoded visually imagined objects and the achieved classification performance. These results suggest the feasibility of using our proposed approach to increase the control's dimensions of EEG-based BCI systems to better assist individuals with mental disorders. To the best of our knowledge, this is the first study that explores the use of the Choi-Williams distribution to analyze EEG signals in the joint time-frequency domain for decoding visually imagined objects.

The rest of this paper is organized as follows: In Section II, we describe the acquired EEG dataset, time-frequency analysis of the recorded EEG signals, TFFs extracted from the Choi-Williams distribution, decoding visually imagined objects, and performance evaluation analyses and metrics. In Sections III and IV, we present and discuss the results obtained for each evaluation analysis, and we compare the performance of our proposed approach with the performance

R. Alazrai *et al.*: Time-Frequency Distribution-Based Approach for Decoding Visually Imagined Objects Using EEG Signals

IEEE Access

of other existing approaches. Finally, the conclusion is provided in Section V.

II. MATERIALS AND METHODS
A. SUBJECTS
Sixteen healthy subjects (two females, 14 males; age range of $18 - 26$ years; mean $\pm$ standard deviation age of 20.4 ± 2.1 years) with normal vision and no neurological disorders volunteered to participate in this study. We refer to the sixteen subjects as S_1 to S_{16}. Before participating in the study, each subject received a thorough written and oral explanation of the experimental procedure and signed a written consent form. The experimental procedure of this study was approved by the Research Ethics Committee at the German Jordanian University and conducted according to the principles presented in the Declaration of Helsinki.

B. STIMULI
The objects to be imagined are grouped into four categories. The first category consists of visual stimuli related to nature. Specifically, the first category comprises four objects, namely a green apple, a yellow banana, a brown elephant, and a blue bird. For each object in the first category, an image of size 9 cm × 9 cm, resolution 2000 × 2000 pixels, and white background was used as a visual stimulus (Fig. 1A). These images were acquired from the Bank of Standardized Stimuli (BOSS) [45]. The second category comprises visual stimuli of the decimal digits $(0 - 9)$. An image of size 6.4 cm × 3.5 cm and white background was created and used as a visual stimulus for each decimal digit. The decimal digit within each image was typed using a black, bold, Arial font of size 150 pt (Fig. 1B). The third category comprises visual stimuli of the English alphabet $(A - Z)$. An image of size 6.4 cm × 4.3 cm and white background was created and used as a visual stimulus for each letter. The letter within each image was typed in an uppercase format using a black, bold, Arial font of size 150 pt (Fig. 1C). Finally, the fourth category consists of visual stimuli for 16 arrows that have four orientations, including upward, rightward, downward, and leftward, and four colors, including white, blue, red, and green. An image of size 5 cm × 7 cm and white background was created and used as a visual stimulus for each of the 16 arrows (Fig. 1D). Figure 1 describes the objects within each of the four categories and shows the image used as a visual stimulus during the imagination of each object.

C. EXPERIMENTAL PROTOCOL
At the beginning of the experiment, each subject was seated on a comfortable chair at a viewing distance of approximately 100 cm from a computer monitor placed on top of a desk. The computer monitor was employed to display visual stimuli associated with the objects presented in Fig. 1, where each visual stimulus notifies the subject to imagine a particular object. During the experiment, the experimenter, EEG acquisition system, and recording station were located behind the subject.

For each trial, a white screen is displayed on the monitor for five seconds, during which the subject is asked to relax, keep her/his eyes open, and rest her/his hands on the desk located in front of her/him. After the relaxing period, a visual stimulus is presented in the center of the monitor against a white background for five seconds. During the visual stimulus period, the subject is asked to carefully observe the picture of the object presented on the screen located in front of her/him. After that, a black screen is displayed on the monitor to indicate the beginning of the visual imagery period. During the visual imagery period, the subject is asked to imagine the object presented during the visual stimulus period while keeping her/his eyes closed [39], [46]–[49]. The duration of the visual imagery period is eight seconds. Finally, a beep sound is used to alert the subject about the end of the trial and to open her/his eyes. Figure 2 shows the timing diagram for each recorded trial.

In this study, the number of trials recorded for each subject while imagining each individual object in categories 1, 2, and 3 is equal to 7 trials. Furthermore, the number of trials recorded for each subject while imagining each object in category 4 is equal to 10 trials. Hence, for each subject, the total number of recorded trials is equal to 440 trials (*i.e.*, (7 trials × 4 objects in category 1) + (7 trials × 10 objects in category 2) + (7 trials × 26 objects in category 3) + (10 trials × 16 objects in category 4)). The average duration of the experiments for each subject was approximately 6 hours divided into 3 to 4 separate recording sessions that were conducted on different days. The duration of each recording session was within the range of $1.5 - 2$ hours, including the time required to mount the EEG cap and electrodes on the scalp of the subject, the time needed to perform the experiments, and the break times granted to the subject upon her/his request during the recording session. During each recording session, each subject was asked to immediately notify the experimenter about any fatigue or uncomfortable feeling so that the experimenter will immediately stop the recording, delete the last recorded trial, and reschedule another recording session for the subject to continue the experiments.

D. EEG SIGNALS ACQUISITION AND PREPROCESSING
The Biosemi ActiveTwo EEG recording system (Biosemi B.V., Amsterdam, Netherlands) was employed to record the EEG signals at a sampling frequency of 2048 Hz. In particular, 16 Ag/AgCL active electrodes were mounted in an elastic cap according to the international $10-20$ electrode placement system. The utilized electrodes are mounted on the scalp at the following locations: Fp_1, Fp_2, F_3, F_z, F_4, T_7, T_8, C_3, C_z, C_4, P_3, P_z, P_4, O_1, O_z, and O_2. These EEG electrodes are referenced to the common mode sense (CMS)/ driven right leg (DRL) at the C_1 and C_2 locations. During the recording of each trial, the offset of each electrode was kept below 40 mV.

The recorded EEG signals were pre-processed by applying a bandpass filter with a bandwidth of $1 - 45$ Hz, re-referencing all EEG electrodes to the EEG electrode at

IEEE *Access*

R. Alazrai *et al.*: Time-Frequency Distribution-Based Approach for Decoding Visually Imagined Objects Using EEG Signals

(A)

Category 1			
Object number	Object description	Object name	Object's visual cue image
1	Green apple	Apple	
2	Yellow banana	Banana	
3	Brown elephant	Elephant	
4	Blue bird	Bird	

(B)

Category 2			
Object number	Object description	Object name	Object's visual cue image
1	Decimal digit 0	Zero	**0**
2	Decimal digit 1	One	**1**
3	Decimal digit 2	Two	**2**
4	Decimal digit 3	Three	**3**
5	Decimal digit 4	Four	**4**
6	Decimal digit 5	Five	**5**
7	Decimal digit 6	Six	**6**
8	Decimal digit 7	Seven	**7**
9	Decimal digit 8	Eight	**8**
10	Decimal digit 9	Nine	**9**

(C)

Category 3			
Object number	Object description	Object name	Object's visual cue image
1	Capital letter A	A	**A**
2	Capital letter B	B	**B**
3	Capital letter C	C	**C**
4	Capital letter D	D	**D**
5	Capital letter E	E	**E**
6	Capital letter F	F	**F**
7	Capital letter G	G	**G**
8	Capital letter H	H	**H**
9	Capital letter I	I	**I**
10	Capital letter J	J	**J**
11	Capital letter K	K	**K**
12	Capital letter L	L	**L**
13	Capital letter M	M	**M**
14	Capital letter N	N	**N**
15	Capital letter O	O	**O**
16	Capital letter P	P	**P**
17	Capital letter Q	Q	**Q**
18	Capital letter R	R	**R**
19	Capital letter S	S	**S**
20	Capital letter T	T	**T**
21	Capital letter U	U	**U**
22	Capital letter V	V	**V**
23	Capital letter W	W	**W**
24	Capital letter X	X	**X**
25	Capital letter Y	Y	**Y**
26	Capital letter Z	Z	**Z**

(D)
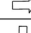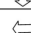
Category 4			
Object number	Object description	Object name	Object's visual cue image
1	Unfilled, upward pointing arrow	Arrow1	⇧
2	Unfilled, rightward pointing arrow	Arrow2	⇨
3	Unfilled, downward pointing arrow	Arrow3	⇩
4	Unfilled, leftward pointing arrow	Arrow4	⇦
5	Blue, upward pointing arrow	Arrow5	⬆
6	Red, upward pointing arrow	Arrow6	⬆
7	Green, upward pointing arrow	Arrow7	⬆
8	Blue, rightward pointing arrow	Arrow8	➡
9	Red, rightward pointing arrow	Arrow9	➡
10	Green, rightward pointing arrow	Arrow10	➡
11	Blue, downward pointing arrow	Arrow11	⬇
12	Red, downward pointing arrow	Arrow12	⬇
13	Green, downward pointing arrow	Arrow13	⬇
14	Blue, leftward pointing arrow	Arrow14	⬅
15	Red, leftward pointing arrow	Arrow15	⬅
16	Green, leftward pointing arrow	Arrow16	⬅

FIGURE 1. The four categories of the imagined objects. (A) The first category consists of four objects, namely a green apple, a yellow banana, a brown elephant, and a blue bird. (B) The second category comprises the decimal digits ($0 - 9$). (C) The third category contains the English alphabet (capital letters ($A - Z$)). (D) The fourth category comprises 16 arrows that have four orientations and four colors.

position C_z [50], correcting the baseline using the last 500 ms of the relax period within each trial [41], downsampling the EEG signals to 256 Hz, and reducing the muscular and ocular artifacts from the acquired EEG signals using the automatic artifact rejection (AAR) open-source MATLAB toolbox [51]. The EEG electrode at position C_z, which was used for re-referencing, was eliminated from the following analysis [41], [50].

E. TIME-FREQUENCY ANALYSIS OF THE EEG SIGNALS
The EEG signals have shown to possess time-varying spectral characteristics (i.e., non-stationary signals) [52], [53].

R. Alazrai *et al.*: Time-Frequency Distribution-Based Approach for Decoding Visually Imagined Objects Using EEG Signals

IEEE*Access*

FIGURE 2. The timing diagram of each recorded trial.

This entails that analyzing the EEG signals in the time-only or frequency-only domains may not be sufficient to capture the non-stationary characteristics of the EEG signals [54]. Indeed, recent studies have indicated that the performance of the EEG signal classification approaches that use features that are extracted from a joint time-frequency domain outperform the performance of the approaches that utilize features that are extracted from the time-only or frequency-only domains [8], [44], [52]. In light of this, we propose to use the Choi-Williams distribution (CWD) [55] to analyze the EEG signals in the joint time-frequency domain. The CWD is a time-frequency distribution that transforms the signal from the time-domain into a joint time-frequency domain that describes the distribution of the energy comprised within the signal over the time and frequency domains [55], [56].
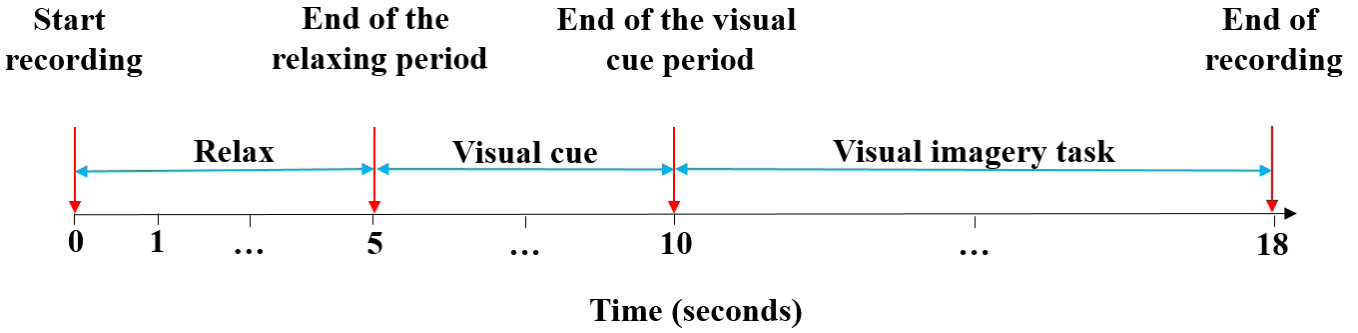
To compute the CWD of the EEG signals, we have implemented a sliding window to divided the EEG signal associated with each EEG channel into a set of overlapped segments. In particular, the size of the sliding window is set to 256 samples, which represents the length of each EEG segment, and the overlap between any two consecutive window positions is set to 128 samples. Then, the CWD of an EEG segment, $z(t)$, denoted as CWD_z, can be computed as follows [44], [55]:

$$CWD_z(t,f) = \int_{-\infty}^{\infty}\int_{-\infty}^{\infty} \Gamma(\theta, \eta)\mathcal{A}_{y(t)}(\theta, \eta)e^{-j2\pi f \eta - j2\pi t\theta}\,\partial_\eta\,\partial_\theta,$$

(1)

where $y(t)$, $\mathcal{A}_{y(t)}(\theta, \eta)$, and $\Gamma(\theta, \eta)$ represent the analytic signal computed for the EEG segment $z(t)$, the ambiguity function computed for $y(t)$, and the time-frequency smoothing kernel of the CWD, respectively. Specifically, the analytic signal $y(t)$ can be computed as follows:

$$y(t) = z(t) + j\mathcal{H}\{z(t)\},$$

(2)

where $\mathcal{H}\{\cdot\}$ is the Hilbert transform [57]. The ambiguity function $\mathcal{A}_{y(t)}(\theta, \eta)$ is defined as the Fourier transform of the auto-correlation function computed for $y(t)$, which can be expressed as follows [58], [59]:

$$\mathcal{A}_{y(t)}(\theta, \eta) = \int_{-\infty}^{\infty} y(t + \frac{\eta}{2})y^*(t - \frac{\eta}{2})e^{j2\pi\theta t}\,\partial t,$$

(3)

where $y^*(\cdot)$ is the complex conjugate of $y(\cdot)$. Finally, the time-frequency smoothing kernel of the CWD can be expressed as follows [55]:

$$\Gamma(\theta, \eta) = \exp\left(-\frac{\theta^2\eta^2}{r^2}\right),$$

(4)

where $r > 0$ is a parameter that controls the amount of smoothing applied to the cross-terms comprised in the computed CWD_z and its value was experimentally set to 0.5.

In this study, we have utilized the HOSA toolbox [60] to compute the CWD of the EEG segments. Specifically, for each EEG segment, the dimensionality of the computed CWD is equal to $\tau = 256 \times \omega = 512$, where τ and ω represent the number of samples along the time and frequency axes, respectively. Figure 3 presents the CWD computed for four EEG segments that were extracted from four different trials that were recorded for the second subject recruited in this study while imagining the following four objects: a green apple, digit zero, capital letter A, and Arrow1.

F. FEATURE EXTRACTION
The CWD computed for an EEG segment provides a high-resolution time-frequency description of the spectral variations in the EEG signals over time. Nonetheless, the number of samples comprised within the CWD computed for each EEG segment is larger than the number of samples within the EEG segment. Moreover, the CWD computed for each EEG segment contains a large number of points in the time-frequency plane with values that are equal or very close to zero. Therefore, it is important to extract highly discriminatory features from the CWD computed for each EEG segment to reduce the dimensionality of the CWD and build classifiers that can accurately distinguish between the EEG segments that are associated with different visually imagined objects.

In this study, we extract twelve time-frequency features (TFFs) from the CWD computed for each EEG segment. These features are: the sum of the logarithmic amplitudes (F_1), median absolute deviation (F_2), root mean square value (F_3), inter-quartile range (F_4), mean (F_5), variance (F_6), skewness (F_7), kurtosis (F_8), flatness (F_9), flux (F_{10}), normalized Renyi entropy (F_{11}), and energy concentration (F_{12}) of the CWD computed for an EEG segment. Table 1 provides a mathematical description for each of the twelve TFFs

IEEE *Access*

R. Alazrai *et al.*: Time-Frequency Distribution-Based Approach for Decoding Visually Imagined Objects Using EEG Signals
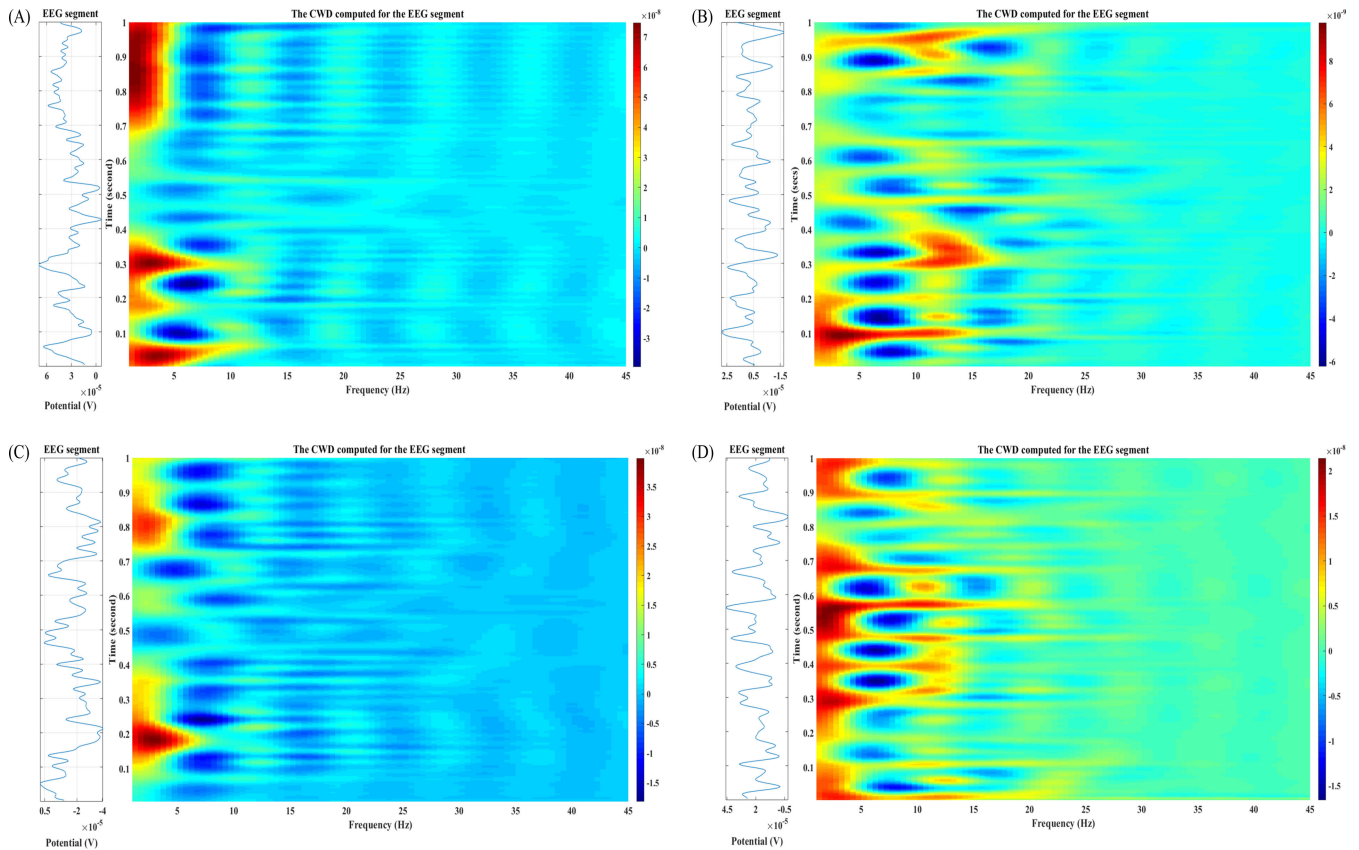

FIGURE 3. Illustration of the computed CWD for different EEG segments. (A)-(D) represent the CWD computed for EEG segments that were extracted from the EEG electrode mounted at position Fp_2 on the scalp of the second subject while imagining a green apple, digit zero, capital letter A, and Arrow1, respectively.

extracted from the CWD computed for each EEG segment. The features $F_1 - F_8$ provide statistical measurements that are extracted from the amplitude of the points in the CWD computed for each EEG segment, while the features $F_8 - F_{12}$ provide spectral measurements that quantify the spread of the energy in the time-frequency plane of the CWD computed for each EEG segment. Further details regarding the computation procedure and interpretation of each of the aforementioned twelve features can be found in our pervious work [5], [8].

The number of EEG segments that are extracted at each position of the sliding window is equal to the number of the utilized EEG channels (i.e., 15 EEG channels). Therefore, the total number of features that are extracted at each position of the sliding window is equal to 180 features (i.e., 15 EEG segments × 12 features per EEG segment). These TFFs, which are extracted from the EEG segments that are associated with a particular position of the sliding window, are grouped to construct a feature vector.

G. CLASSIFICATION OF VISUALLY IMAGINED OBJECTS

Previous studies have indicated that different subjects have different abilities to perform imagery tasks [12], [18], [53], [61]. This suggests the construction of subject-specific classifiers to distinguish between the EEG signals associated with

various imagined objects [2], [6], [8], [40]. In this study, we have implemented five classification scenarios for each subject. The first, second, third, fourth, and fifth classification scenarios aim to construct classifiers that can distinguish between the EEG signals associated with the objects in category 1, category 2, category 3, category 4, and all combined categories, respectively. In particular, we utilized the feature vectors that are extracted from the trials of each subject to build and train a multi-class support vector machine (SVM) classifier with the Gaussian radial basis function (RBF) kernel [62] for each one of the five classification scenarios.

The reasons behind using a multi-class SVM classifier are summarized in two folds: (1) The majority of the previous studies that investigated the decoding of visually imagined objects by analyzing the EEG signals, such as the studies presented in [2], [12], [40], [41], have utilized SVM classifiers to decode the visually imagined objects. Hence, the use of the SVM classifier can facilitate the comparison between the performance of our proposed approach and the performance reported in these previous studies as described in section IV. (2) Previous studies have shown that utilizing the SVM classifier with RBF kernel can be more effective than generative models for supervised learning problems [63]. Moreover, using the SVM classifier with RBF

R. Alazrai *et al.*: Time-Frequency Distribution-Based Approach for Decoding Visually Imagined Objects Using EEG Signals

IEEE *Access*

TABLE 1. The twelve TFFs extracted from the CWD computed for each EEG segment.

Feature	Mathematical description	
Sum of the logarithmic amplitudes (F_1)	$F_1 = \sum_{t=1}^{\tau} \sum_{f=1}^{\omega} \log \left(\left| CWD_z(t,f) \right| \right)$	(5)
Median absolute deviation (F_2)	$F_2 = \frac{1}{\tau \times \omega} \sum_{t=1}^{\tau} \sum_{f=1}^{\omega} \left| CWD_z(t,f) - \frac{1}{\tau \times \omega} \sum_{t=1}^{\tau} \sum_{f=1}^{\omega} CWD_z(t,f) \right|$	(6)
Root mean square value (F_3)	$F_3 = \sqrt{\left(\sum_{t=1}^{\tau} \sum_{f=1}^{\omega} \left(CWD_z(t,f) \right)^2 \right) / (\tau \times \omega)}$	(7)
Inter-quartile range (F_4)	$F_4 = \frac{1}{\omega} \sum_{f=1}^{\omega} \left(CWD_z\left(\frac{3(\tau+1)}{4}, f \right) - CWD_z\left(\frac{(\tau+1)}{4}, f \right) \right)$	(8)
Mean (F_5)	$F_5 = \frac{1}{\tau \times \omega} \sum_{t=1}^{\tau} \sum_{f=1}^{\omega} CWD_z(t,f)$	(9)
Variance (F_6)	$F_6 = \frac{1}{\tau \times \omega} \sum_{t=1}^{\tau} \sum_{f=1}^{\omega} \left(CWD_z(t,f) - F_5 \right)^2$	(10)
Skewness (F_7)	$F_7 = \frac{1}{\tau \times \omega \times (F_6)^{3/2}} \sum_{t=1}^{\tau} \sum_{f=1}^{\omega} \left(CWD_z(t,f) - F_5 \right)^3$	(11)
Kurtosis (F_8)	$F_8 = \frac{1}{\tau \times \omega \times (F_6)^2} \sum_{t=1}^{\tau} \sum_{f=1}^{\omega} \left(CWD_z(t,f) - F_5 \right)^4$	(12)
Flatness (F_9)	$F_9 = \tau \times \omega \times \frac{\prod_{t=1}^{\tau} \prod_{f=1}^{\omega} (\left| CWD_z(t,f) \right|)^{1/\tau \times \omega}}{\sum_{t=1}^{\tau} \sum_{f=1}^{\omega} (\left| CWD_z(t,f) \right|)}$	(13)
Flux (F_{10})	$F_{10} = \sum_{t=1}^{\tau-l} \sum_{f=1}^{\omega-k} \left(CWD_z(t+l, f+k) - CWD_z(t,f) \right), l = k = 1$	(14)
Normalized Renyi entropy (F_{11})	$F_{11} = \frac{1}{1-\nu} \log_2 \sum_{t=1}^{\tau} \sum_{f=1}^{\omega} \left(\frac{CWD_z(t,f)}{\sum_{t=1}^{\tau} \sum_{f=1}^{\omega} CWD_z(t,f)} \right)^{\nu}, \nu = 3$	(15)
Energy concentration (F_{12})	$F_{12} = \left(\sum_{t=1}^{\tau} \sum_{f=1}^{\omega} \sqrt{\left| CWD_z(t,f) \right|} \right)^2$	(16)

kernel can achieve better performance and generalization compared with other state-of-the-art classifiers, such as Naive Bayes, k-nearest neighbors (k-NN), and neural networks [52], [64]. In addition, many previous EEG-based studies that were focused on decoding imagery tasks have indicated that the classification performance obtained using the SVM classifier outperforms the classification performance achieved by other classifiers, such as linear discriminant analysis (LDA) and linear regression (LR) [65], [66].

A one-against-one voting scheme [67], [68] is employed to implement the multi-class SVM classifier for each subject, in which a set of $n(n - 1)/2$ binary SVM classifiers are trained to construct a n-class SVM classifier. In this study, n is equal to 4, 10, 26, 16, and 56 for the first, second, third, fourth, and fifth classification scenarios, respectively. Moreover, a grid-based search is performed to tune the parameters of the constructed multi-class SVM classifiers for each subject and each classification scenario, including

IEEE *Access*

R. Alazrai *et al.*: Time-Frequency Distribution-Based Approach for Decoding Visually Imagined Objects Using EEG Signals

the regularization parameter (C) and the kernel parameter (γ). In particular, we perform a grid-based search along two directions to determine the values of γ and C for each multi-class SVM classifier. In the first direction, we varied the value of the parameter γ to the following range: {0.0001, 0.001, 0.01, 0.1, 0.5, 1, 1.5, 5, 10}. Furthermore, in the second direction, we varied the value of the parameter C in the following range: {0.01, 0.5, 1, 5, 10, 50, 70}. For each subject and each classification scenario, the tuned parameters of the SVM model are selected as the values of γ and C that maximize the average classification accuracy [69].

A ten-fold cross-validation procedure is employed to train and test the multi-class SVM classifiers which are constructed for each subject and each classification scenario [8], [66], [70]. Specifically, for a particular subject and classification scenario, 90% of the feature vectors associated with the objects are randomly selected and used for training, while the remaining 10% of the feature vectors are used for testing. The aforementioned ten-fold cross-validation procedure is repeated ten times, and the overall classification performance is computed for each subject and each classification scenario by averaging the results obtained from each repetition [5], [6].

H. PERFORMANCE EVALUATION ANALYSES AND METRICS

In this section, we describe the implementation of two performance evaluation analyses, namely the channel- and feature-based analyses, that investigate the effect of the utilized EEG channels and TFFs on the performance of each of the five classification scenarios. We also provide a description of the performance evaluation metrics used to quantify the classification performance obtained based on each evaluation analyses for each of the five classification scenarios.

1) CHANNEL-BASED PERFORMANCE EVALUATION ANALYSIS (CBA)

The objective of the CBA is to investigate the effect of the utilized EEG electrodes on the accuracy of distinguishing between the EEG signals that are associated with different visually imagined objects. To implement this analysis, we have constructed ten different groups of EEG electrodes that cover various regions of the brain. Then, for each subject, we have utilized the EEG electrodes comprised within each of the ten groups to extract the feature vectors from the EEG segments at each window position and perform the five classification scenarios described in subsection II-G. Table 2 describes each of the ten groups of electrodes along with the dimensionality of the feature vectors extracted from the EEG electrodes comprised within each group.

2) FEATURE-BASED PERFORMANCE EVALUATION ANALYSIS (FBA)

The objective of the FBA is to study the effect of reducing the number of TFFs, which are extracted from the EEG segments at each position of the sliding window, on the accuracy of decoding the different visually imagined objects. In this

analysis, we utilize the minimum redundancy maximum relevance (mRMR) feature selection approach [71] to reduce the dimensionality of the feature vectors extracted from the group of EEG electrodes that achieved the best classification performance in the CBA. The mRMR feature selection approach uses the mutual information to select a subset of the TFFs that have the maximum correlation (i.e., relevance) with a particular imagined object and the minimum correlation (i.e., redundancy) between the selected features. The selected TFFs are ranked in descending order according to the minimum-redundancy maximum-relevance basis [71].

To implement the FBA, the mRMR approach was applied for each subject and each classification scenario to generate five different subsets of feature vectors, namely subset 1, subset 2, subset 3, subset 4, and subset 5. In particular, the first, second, third, fourth, and fifth subsets of feature vectors comprise the selected highest-ranking 5%, 10%, 25%, 50%, and 75% of the TFFs extracted from the EEG electrodes of G_{10}, respectively. Finally, the performance of each classification scenario is assessed using each of the five subsets of feature vectors to determine the impact of reducing the number of features on the accuracy of decoding the visually imagined objects.

3) PERFORMANCE EVALUATION METRICS

For each performance evaluation analysis, the average classification performance is computed across the ten train-test repetitions (i.e., the ten repetitions of the ten-fold cross-validation procedure) in terms of two standard evaluation metrics, namely the average classification accuracy (CA) and average $F_1 - Score$ (F_1). In particular, the average CA and F_1 values are computed for each subject and each classification scenario across the ten train-test repetitions as follows [72]:

$$CA = \frac{1}{K} \sum_{k=1}^{K} \left(\frac{\sum_{l=1}^{L} tp_l}{\text{no. of testing samples in the fold k}} \right) \times 100\%,$$

$$\tag{17}$$

$$F_1 = \frac{1}{K} \left(\frac{1}{L} \sum_{l=1}^{L} \left(2 \times \frac{(RE_{l,k} \times PR_{l,k})}{(RE_{l,k} + PR_{l,k})} \right) \right) \times 100\%, \tag{18}$$

where $K = 10$ represents the number of repetitions of the ten-fold cross-validation procedure, L represents the number of objects associated with a particular classification scenario, tp_l represents the number of true positive samples that belong to object l within a specific classification scenario, $RE_{l,k}$ and $PR_{l,k}$ are the recall and precision of class l computed for the testing fold k, respectively. After that, for each classification scenario, we compute the mean $\pm$ standard deviation values of the average CAs and $F_1 - Scores$ over the 16 subjects and report these results in the next section.

III. EXPERIMENTAL RESULTS
A. RESULTS OF THE CBA
Table 3 shows the average CA and F_1 values computed for each of the five classification scenarios and each of the

TABLE 2. The groups of the EEG electrodes considered in the CBA.

Group	Description	EEG electrodes	Dimensionality of the extracted feature vector from the EEG segments at each position of the sliding window
Group 1 (G_1)	This group consists of six different subgroups of EEG electrodes that cover six different regions of the brain. These subgroups are: 1. Subgroup 1 covers the central region. 2. Subgroup 2 covers the frontal pole region. 3. Subgroup 3 covers the frontal region. 4. Subgroup 4 covers the temporal region. 5. Subgroup 5 covers the parietal region. 6. Subgroup 6 covers the occipital region.	C_3 and C_4 Fp_1 and Fp_2 F_3, F_z, and F_4 T_7 and T_8 P_3, P_z, and P_4 O_1, O_z, and O_2	2 electrodes × 12 features = 24 2 electrodes × 12 features = 24 3 electrodes × 12 features = 36 2 electrodes × 12 features = 24 3 electrodes × 12 features = 36 3 electrodes × 12 features = 36
Group 2 (G_2)	This group includes the EEG electrodes in the frontal pole and frontal regions.	Fp_1, Fp_2, F_3, F_z, and F_4	5 electrodes × 12 features = 60
Group 3 (G_3)	This group includes the EEG electrodes in the temporal and occipital regions.	T_7, T_8, O_1, O_z, and O_2	5 electrodes × 12 features = 60
Group 4 (G_4)	This group includes the EEG electrodes in the frontal pole, frontal, and parietal regions.	Fp_1, Fp_2, F_3, F_z, F_4, P_3, P_z, and P_4	8 electrodes × 12 features = 96
Group 5 (G_5)	This group includes the EEG electrodes in the temporal, parietal, and occipital regions.	T_7, T_8, P_3, P_z, P_4, O_1, O_z, and O_2	8 electrodes × 12 features = 96
Group 6 (G_6)	This group includes the EEG electrodes in the frontal pole, frontal, temporal, and parietal regions.	Fp_1, Fp_2, F_3, F_z, F_4, T_7, T_8, P_3, P_z, and P_4	10 electrodes × 12 features = 120
Group 7 (G_7)	This group includes the EEG electrodes in the central, temporal, parietal, and occipital regions.	C_3, C_4, T_7, T_8, P_3, P_z, P_4, O_1, O_z, and O_2	10 electrodes × 12 features = 120
Group 8 (G_8)	This group includes the EEG electrodes in the frontal pole, frontal, parietal, and occipital regions.	Fp_1, Fp_2, F_3, F_z, F_4, P_3, P_z, P_4, O_1, O_z, and O_2	11 electrodes × 12 features = 132
Group 9 (G_9)	This group includes the EEG electrodes in the frontal pole, frontal, temporal, parietal, and occipital regions.	Fp_1, Fp_2, F_3, F_z, F_4, T_7, T_8, P_3, P_z, P_4, O_1, O_z, and O_2	13 electrodes × 12 features = 156
Group 10 (G_{10})	This group includes all the EEG electrodes.	C_3, C_4, Fp_1, Fp_2, F_3, F_z, F_4, T_7, T_8, P_3, P_z, P_4, O_1, O_z, and O_2	15 electrodes × 12 features = 180

TABLE 3. The results of the CBA. The highest average CA and F_1 values obtained for each classification scenario are highlighted using bold font. STD represents the standard deviation.

Groups of EEG electrodes		Classification scenario 1				Classification scenario 2				Classification scenario 3				Classification scenario 4				Classification scenario 5			
		CA	STD	F_1	STD	CA	STD	F_1	STD	CA	STD	F_1	STD	CA	STD	F_1	STD	CA	STD	F_1	STD
G_1	Subgroup 1	70.38	14.94	69.58	15.16	46.61	16.67	45.47	16.93	37.37	12.56	36.35	12.36	49.40	15.92	48.86	15.94	36.41	11.72	35.03	11.48
	Subgroup 2	90.06	6.43	89.60	6.67	77.44	13.30	76.94	13.40	66.87	18.28	66.01	18.35	71.83	13.27	71.32	13.31	59.22	14.95	58.16	14.93
	Subgroup 3	71.08	12.27	70.02	12.58	53.90	16.73	52.92	16.95	44.27	13.75	43.28	13.60	52.83	12.95	52.25	12.94	40.51	11.88	39.14	11.88
	Subgroup 4	69.83	13.53	68.91	13.71	46.22	16.34	45.32	16.52	34.88	10.39	33.87	10.38	46.15	12.57	45.36	12.61	32.78	10.17	31.47	10.13
	Subgroup 5	59.23	14.02	58.13	14.12	40.81	14.41	39.54	14.58	30.30	12.40	29.45	12.42	41.51	13.85	40.97	13.84	28.75	10.83	27.56	10.78
	Subgroup 6	65.38	12.07	64.13	12.20	40.80	17.49	39.74	17.54	29.75	15.21	29.09	15.20	40.83	14.30	40.29	14.27	28.16	12.52	26.97	12.53
G_2		92.80	3.17	92.33	3.41	84.08	4.85	83.56	4.98	78.69	7.56	77.96	7.67	83.81	5.21	83.47	5.28	74.44	6.26	73.44	6.36
G_3		80.84	6.17	80.20	6.25	58.58	9.40	57.64	9.61	49.10	8.11	48.28	8.10	59.36	7.97	58.64	7.95	48.84	7.68	47.55	7.68
G_4		93.00	3.46	92.68	3.49	85.33	4.91	84.78	5.02	79.29	7.30	78.61	7.46	83.98	5.04	83.52	5.15	75.69	6.32	74.83	6.50
G_5		83.56	5.96	83.04	6.08	66.65	8.68	65.69	8.86	52.04	7.96	51.01	8.06	67.80	8.11	67.21	8.19	57.19	7.45	55.92	7.48
G_6		94.14	2.94	93.75	3.00	86.96	4.63	86.37	4.78	82.24	7.08	81.52	7.24	86.62	5.20	86.36	5.26	78.61	5.82	77.72	5.98
G_7		86.92	5.11	86.45	5.15	71.08	7.64	70.34	7.79	65.51	7.51	64.70	7.56	74.31	7.97	73.81	8.03	64.33	7.25	63.12	7.29
G_8		94.07	3.39	93.60	3.45	85.18	4.42	84.63	4.65	79.16	6.52	78.56	6.69	84.70	4.54	84.36	4.63	76.89	5.62	75.93	5.75
G_9		95.18	2.61	94.85	2.72	86.82	4.47	86.33	4.62	81.79	6.22	81.10	6.27	86.43	4.76	86.10	4.87	79.50	5.55	78.71	5.69
G_{10}		**95.73**	2.07	**95.57**	2.17	**88.21**	3.86	**87.64**	4.08	**83.59**	6.32	**82.95**	6.39	**87.68**	4.91	**87.42**	4.96	**81.57**	5.31	**80.82**	5.50

ten different groups of EEG electrodes, which are depicted in 2. The CA and F_1 values presented in Table 3 are computed over all subjects and all objects within each classification scenario. In particular, for G_1, the average CA and F_1 values computed for each of the five classification scenarios based on the TFFs extracted from the EEG electrodes comprised in subgroup 2, which cover the frontal pole region of the brain, are substantially higher than the average CA and F_1 values obtained based on the TFFs extracted from the EEG electrodes comprised within each of the other five different subgroups of G_1. Specifically, using subgroup 2, the average CA/F_1 values achieved for the first, second, third, fourth, and fifth classification scenarios were 90.06%/89.60%, 77.44%/76.94%, 66.87%/66.01%, 71.83%/71.32%, and 59.22%/58.16%, respectively. Moreover, the results presented in Table 3 show that the average

IEEE *Access*

R. Alazrai *et al.*: Time-Frequency Distribution-Based Approach for Decoding Visually Imagined Objects Using EEG Signals

CA and F_1 values computed for each of the five classification scenarios based on the TFFs extracted from the EEG electrodes of subgroup 1, subgroup 3, and subgroup 4 are relatively close to each other and are higher than the average *CA* and F_1 values obtained based on using the TFFs extracted from the EEG electrodes of subgroup 5 and subgroup 6.

The average *CA* and F_1 values computed for each of the five classification scenarios based on the TFFs extracted from the EEG electrodes comprised in G_2, which covers the frontal pole and frontal regions of the brain, are higher than the average *CA* and F_1 values obtained based on the TFFs extracted from the EEG electrodes comprised within each of the six different subgroups of G_1. Specifically, using G_2, the average CA/F_1 values achieved for the first, second, third, fourth, and fifth classification scenarios were 92.80%/92.33%, 84.08%/83.56%, 78.69%/77.96%, 83.81%/83.47%, and 74.44%/73.44%, respectively. Similarly, for each of the five classification scenarios, using the TFFs extracted from the EEG electrodes in G_3, which cover the temporal and occipital regions of the brain, achieved an average *CA* and F_1 values that are substantially higher than the average *CA* and F_1 values achieved using the TFFs extracted from the EEG electrodes of subgroup 4 and subgroup 6, which cover the temporal region of the brain and the occipital region of the brain, respectively.

Table 3 also shows that using the TFFs extracted from the EEG electrodes of G_4, which cover the frontal pole, frontal, and parietal regions of the brain, achieved an average *CA* and F_1 values that are slightly higher than the average *CA* and F_1 values achieved using the TFFs extracted from the EEG electrodes of G_2, which cover only the frontal pole and frontal regions of the brain. Furthermore, using the TFFs extracted from the EEG electrodes of G_5, which cover the temporal, parietal, and occipital regions of the brain, achieved an average *CA* and F_1 values that are higher than the average *CA* and F_1 values achieved using the TFFs extracted from the EEG electrodes of G_3, which cover the temporal and occipital regions of the brain. In addition, the average *CA* and F_1 values obtained for each classification scenario using the TFFs extracted from the EEG electrodes of G_6, which cover the frontal pole, frontal, temporal, and parietal regions of the brain, are substantially higher than the average *CA* and F_1 values obtained using the TFFs extracted from the EEG electrodes of G_5, which cover the temporal, parietal, and occipital regions of the brain. Moreover, the average *CA* and F_1 values obtained for each classification scenario using the TFFs extracted from the EEG electrodes of G_7, which cover the central, temporal, parietal, and occipital regions of the brain, outperform the average *CA* and F_1 values obtained using the TFFs extracted from the EEG electrodes of G_5, which cover the temporal, parietal, and occipital regions of the brain. At the same time, the average *CA* and F_1 values obtained using the TFFs extracted from the EEG electrodes of G_6 outperform the average *CA* and F_1 values obtained using the TFFs extracted from the EEG electrodes of G_7.

The average *CA* and F_1 values computed for each classification scenario based on the TFFs extracted from the EEG electrodes of G_8, which cover the frontal pole, frontal, parietal, and occipital regions of the brain, are slightly lower than the average *CA* and F_1 values obtained for each classification scenario using the TFFs extracted from the EEG electrodes of G_6, which cover the frontal pole, frontal, temporal, and parietal regions of the brain. In addition, for each classification scenario, the average *CA* and F_1 values obtained using the TFFs extracted from the EEG electrodes of G_9, which cover the frontal pole, frontal, temporal, parietal, and occipital regions of the brain, outperform the average *CA* and F_1 values obtained using G_7, which overs the central, temporal, parietal, and occipital regions of the brain, and the average *CA* and F_1 values obtained using G_8, which covers the frontal pole, frontal, parietal, and occipital regions of the brain.

Finally, the best classification performance was achieved using the TFFs extracted from the EEG electrodes of G_{10}, which cover the central, frontal pole, frontal, temporal, parietal, and occipital regions of the brain. In particular, using G_{10}, the average CA/F_1 values achieved for the first, second, third, fourth, and fifth classification scenarios were 95.73%/95.57%, 88.21%/87.64%, 83.59%/82.95%, 87.68%/87.42%, and 81.57%/80.82%, respectively.

To compare the performance results of the proposed approach obtained using G_{10} and the performance results obtained using the other groups of EEG electrodes, we have conducted paired t-tests with significance level of 0.05 that compare the classification accuracies obtained for the five classification scenarios using the TFFs extracted from the EEG electrodes of G_{10} with the classification accuracies obtained for the five classification scenarios using the TFFs extracted from the EEG electrodes of G_9, G_8, G_7, G_6, G_5, G_4, G_3, G_2, and subgroup 2 in G_1, respectively. The computed p values for G_{10} versus G_9, G_8, G_7, G_6, G_5, G_4, G_3, G_2, and subgroup 2 in G_1 were 0.0029, 0.0013, 0.0024, 0.0022, 0.0085, 00099, 0.0036, 0.0056, and 0.0073, respectively. The calculated p values demonstrate that the classification performance obtained using the EEG electrodes of G_10 outperforms significantly the classification performance obtained using the other groups of EEG electrodes.

B. RESULTS OF THE FBA

The results of the CBA, which are shown in Table 3, indicate that using all the TFFs that are extracted from the EEG electrodes of G_{10} achieved the best average *CA* and F_1 values for all the classification scenarios. Therefore, in this subsection, we have selected G_{10}, which comprises all the EEG electrodes, to perform the FBA. The dimensionality of the feature vectors comprised in the first, second, third, fourth, and fifth subsets of feature vectors are equal to 9, 18, 45, 90, and 135, respectively. Table 4 presents the average *CA* and F_1 values computed for each of the five classification scenarios and each of the five different subsets of feature vectors that are extracted from the EEG electrodes of G_{10}.

R. Alazrai *et al.*: Time-Frequency Distribution-Based Approach for Decoding Visually Imagined Objects Using EEG Signals

IEEE *Access*

TABLE 4. The results of the FBA. The highest average *CA* and F_1 values obtained for each classification scenario are highlighted using bold font. STD represents the standard deviation.

Subset of feature vectors	Classification scenarios																			
	Classification scenario 1				Classification scenario 2				Classification scenario 3				Classification scenario 4				Classification scenario 5			
	CA	STD	F_1	STD	CA	STD	F_1	STD	CA	STD	F_1	STD	CA	STD	F_1	STD	CA	STD	F_1	STD
Subset 1	90.98	3.57	90.38	3.74	84.16	5.54	83.47	5.67	79.76	7.45	79.08	7.58	84.51	5.68	84.13	5.76	76.35	7.44	75.54	7.56
Subset 2	94.64	2.54	94.28	2.68	90.97	3.40	90.56	3.55	86.41	6.62	86.07	6.63	91.50	3.77	91.30	3.83	83.92	5.43	83.36	5.64
Subset 3	**96.67**	2.61	**96.37**	2.55	**93.64**	3.62	**93.31**	3.69	**88.95**	4.50	**88.41**	4.65	**92.68**	3.59	**92.28**	3.67	**85.22**	3.74	**84.52**	3.91
Subset 4	95.90	2.54	95.73	2.61	93.10	2.73	92.78	2.85	88.50	5.23	88.11	5.35	91.44	3.72	91.22	3.75	83.06	5.07	82.34	5.22
Subset 5	95.88	2.31	95.87	2.38	90.88	3.51	90.60	3.65	86.65	5.77	86.10	5.87	90.54	4.12	90.40	4.16	82.45	5.16	81.72	5.28

TABLE 5. The selected values of the parameters γ and C for the SVM classifiers constructed for each subject and each classification scenario by using subset 3.

Subject	Classification scenarios									
	Classification scenario 1		Classification scenario 2		Classification scenario 3		Classification scenario 4		Classification scenario 5	
	γ	C	γ	C	γ	C	γ	C	γ	C
S_1	1.00	10.00	0.50	70.00	1.50	50.00	0.50	50.00	0.50	50.00
S_2	0.50	50.00	1.00	50.00	0.50	50.00	1.50	10.00	0.50	50.00
S_3	0.10	70.00	0.10	70.00	0.50	50.00	1.00	10.00	0.50	50.00
S_4	0.10	10.00	1.00	5.00	1.00	50.00	0.50	50.00	1.00	10.00
S_5	0.10	50.00	0.50	10.00	1.00	10.00	1.00	10.00	1.00	50.00
S_6	1.00	10.00	1.00	10.00	1.00	50.00	1.00	50.00	1.00	50.00
S_7	0.50	10.00	1.00	50.00	0.50	50.00	1.00	5.00	0.50	50.00
S_8	0.50	50.00	1.50	5.00	0.50	50.00	0.50	70.00	0.50	70.00
S_9	1.00	10.00	1.00	10.00	0.50	70.00	1.00	10.00	0.50	50.00
S_{10}	0.50	50.00	0.50	70.00	1.50	10.00	0.50	50.00	1.00	70.00
S_{11}	0.10	70.00	0.50	50.00	1.00	10.00	1.50	50.00	0.50	50.00
S_{12}	0.10	70.00	1.00	10.00	0.50	50.00	1.50	50.00	0.50	70.00
S_{13}	0.50	50.00	1.00	50.00	1.00	10.00	0.50	50.00	0.50	70.00
S_{14}	1.00	50.00	0.50	50.00	1.50	5.00	0.50	50.00	0.50	50.00
S_{15}	0.10	50.00	1.00	10.00	0.50	70.00	1.00	50.00	0.50	50.00
S_{16}	0.50	10.00	0.10	70.00	0.50	10.00	1.50	10.00	0.50	50.00

The results presented in Table 4 show that, for all the classification scenarios, the highest average *CA* and F_1 values were achieved using subset 3, which consists of the highest-ranking 25% of the TFFs. Specifically, using the highest-ranking 25% of the TFFs, the average CA/F_1 values achieved for the first, second, third, fourth, and fifth classification scenarios were 96.67%/96.37%, 93.64%/93.31%, 88.95%/88.41%, 92.68%/92.28% and 85.22%/84.52%, respectively. Table 5 shows the selected values of the parameters γ and C, which are obtained using the grid-based search described in section II-G, for the SVM classifiers that are constructed for each subject and each classification scenario based on using the TFFs of subset 3.

To compare the classification results of the proposed approach that are obtained using subset 3 and the results obtained using the other subsets of TFFs, we have conducted paired t-tests with significance level of 0.05 to compare the classification accuracies obtained for the five classification scenarios using subset 3 of the TFFs with the classification accuracies obtained for the five classification scenarios using the TFFs of subset 5, subset 4, subset 2, and subset 1, respectively. The computed p values for subset 3 versus subset 5, subset 4, subset 2, and subset 1 were 0.0040, 0.0301, 0.0174, and 0.00026, respectively. The calculated *p* values demonstrate that the classification performance obtained using subset 3 of the TFFs outperforms significantly the classification performance obtained using the other four subsets of TFFs.

Figure 4 shows the average *CA* values and the corresponding standard deviation values computed for each subject and

each classification scenario using subset 3. Table 6 shows the lowest and highest CA values computed for each of the five classification scenarios using subset 3 along with the subjects associated with these CA values. The results presented in Fig. 4 and Table 6 indicate that the *CA* values computed for each subject using subset 3 are substantially higher than the random classification rates associated with the five classification scenarios, where the random classification rates of the first, second, third, fourth, and fifth classification scenarios are equal to 25%, 10%, 3.8%, 6.25%, and 1.78%, respectively.

To assess the importance of each of the twelve TFFs, for each subject, we have computed the ratio between the number of times a particular TFF was selected for inclusion in each of the five subsets of feature vectors to the dimensionality of the feature vectors comprised within each of the five subsets of feature vectors. Then, for each classification scenario and each subset of feature vectors, the computed selection ratios of each TFF are averaged over all subjects. Table 7 provides the average selection ratio of each of the twelve TFFs computed for each classification scenario and each subset of feature vectors. The results presented in Table 7 show that, for each classification scenario, the use of subset 3 yielded an average selection ratio that is greater than zero for each of the twelve TFFs. In fact, subset 3 consists of the highest-ranking 25% of the TFFs extracted from the EEG electrodes in G_{10}. Therefore, having an average selection ratio that is strictly larger than zero for each of the twelve TFFs implies that each of the twelve TFFs, which is extracted from at least one of the EEG electrodes in G_{10}, is included in subset 3. These results indicate that different TFFs, which are extracted from various EEG electrodes, can capture different characteristics of various visually imagined objects.

Moreover, using subset 3, the average selection ratios computed for each classification scenario, which are provided in Table 7, explicate that the TFFs F_1, F_3, and F_{11} have the highest average selection ratios compared with the other TFFs. This is due to the important characteristics captured by these three TFFs. Specifically, F_1, which is the sum of the logarithmic amplitudes, is a spectral moment-related feature that can quantify the nonlinearity of the energy distribution in the time-frequency plane of the CWD computed for an EEG segment [5], [8], [73]. In addition, F_3, which is the root mean square value, quantifies the variations of the energy distribution in the time-frequency plane of the CWD computed for an EEG segment [5], [8]. Finally, F_{11}, which is
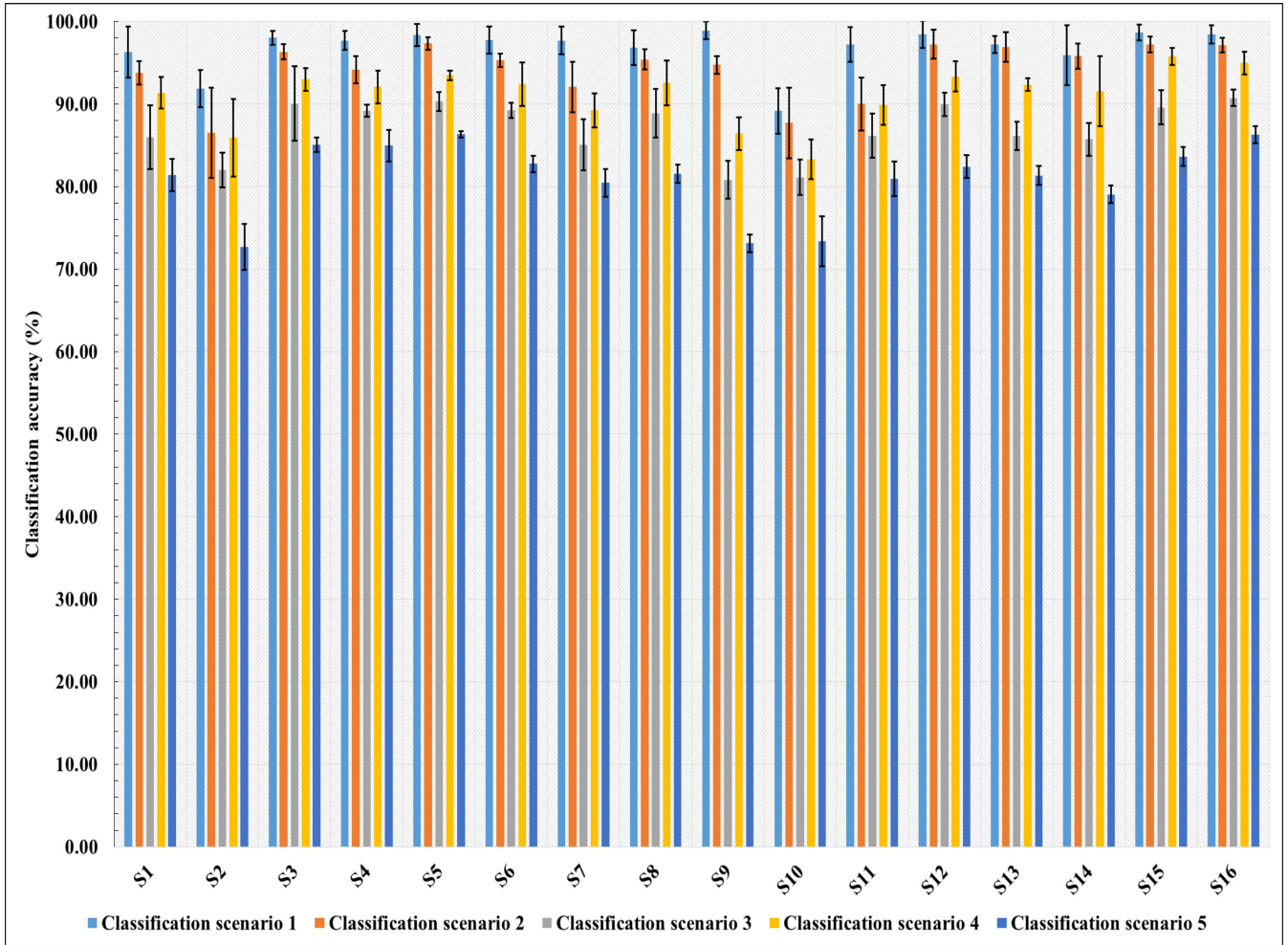
IEEE *Access*

R. Alazrai *et al.*: Time-Frequency Distribution-Based Approach for Decoding Visually Imagined Objects Using EEG Signals

FIGURE 4. The *CA* values computed for each subject and each classification scenario using subset 3 of the feature vectors, which consists of the highest-ranking 25% of the TFFs extracted from the EEG electrodes in G_{10}. The black vertical bars represent the standard deviation in the *CA* values.

TABLE 6. The lowest and highest CA values computed for each of the five classification scenarios using subset 3 along with the subjects associated with these CA values.

	Classification scenario 1	Classification scenario 2	Classification scenario 3	Classification scenario 4	Classification scenario 5
(Lowest CA (%), Subject)	$(89.17, S_{10})$	$(86.53, S_2)$	$(80.8, S_9)$	$(83.33, S_{10})$	$(72.72, S_{10})$
(Highest CA (%), Subject)	$(98.92, S_9)$	$(97.22, S_{12})$	$(90.73, S_{16})$	$(95.78, S_{15})$	$(86.35, S_5)$

the normalized Renyi entropy, characterizes the regularity of the energy spread in the time-frequency plane of the CWD computed for an EEG segment [5], [8], [44], [74].

C. RUNTIME OF THE PROPOSED APPROACH
The proposed approach was implemented on a workstation with a 3.5-GHz Intel Xeon Processor (Intel Corporation, Santa Clara, CA, USA) and 8 GB memory. We provide the runtime of our proposed approach computed for the configuration that yielded the best classification results. In particular, the best classification results were obtained using the EEG electrodes comprised in G_{10}, which contains 15 EEG electrodes, and subset 3 of the TFFs, which contains the highest-ranking 25% of the features (*i.e.*, 45 TFFs).

The average $\pm$ standard deviation time required to train the multi-class SVM classifier constructed for the first, second, third, fourth, and fifth classification scenarios computed across the 16 subjects is equal to 12.79$\pm$1.36 s, 88.56$\pm$6.38 s, 1048.31$\pm$135.06 s, 488.79$\pm$26.03 s, and 5298.74$\pm$653.25 s, respectively.

Despite the relatively long time required during the training process, we only need to learn the multi-class SVM models offline and then identify the testing samples online. Specifically, the average $\pm$ standard deviation time required to compute the CWD of the EEG signal associated with a particular EEG electrode at a particular window position computed across the 16 subjects is equal to 4.55 $\pm$ 1.8 ms. Hence, the average time required to compute the CWD for the EEG

R. Alazrai *et al.*: Time-Frequency Distribution-Based Approach for Decoding Visually Imagined Objects Using EEG Signals

IEEE *Access*

TABLE 7. The average selection ratio (%) of each of the twelve TFFs computed for each classification scenario and each subset of feature vectors.

Classification scenario	Subset of feature vectors	Time-frequency features											
		F_1	F_2	F_3	F_4	F_5	F_6	F_7	F_8	F_9	F_{10}	F_{11}	F_{12}
Classification scenario 1	Subset 1	28.47	2.08	11.11	0.00	3.47	3.47	5.56	6.94	10.42	2.78	16.67	9.03
	Subset 2	23.26	4.51	10.76	0.00	4.51	6.94	6.60	5.56	10.42	6.25	12.85	8.33
	Subset 3	15.83	6.67	10.33	0.56	6.25	9.06	7.50	7.22	9.33	7.92	11.56	7.78
	Subset 4	11.74	7.50	7.85	1.81	7.85	9.24	8.40	8.19	12.43	7.99	8.40	8.61
	Subset 5	9.26	7.69	7.45	6.57	7.96	9.77	7.96	8.84	9.91	8.33	8.61	7.64
Classification scenario 2	Subset 1	40.28	2.78	11.81	1.39	5.56	5.56	1.39	6.25	2.08	5.56	11.81	5.56
	Subset 2	34.72	3.82	10.07	1.04	7.64	5.90	2.78	5.90	2.08	5.90	11.11	9.03
	Subset 3	20.28	7.50	9.89	0.97	7.08	5.69	5.97	6.81	7.22	8.03	10.83	9.72
	Subset 4	13.33	7.92	8.47	1.25	8.19	6.53	7.92	8.13	11.39	8.13	10.42	8.33
	Subset 5	10.23	7.92	8.61	2.87	7.82	8.19	8.66	8.80	10.28	8.89	9.07	8.66
Classification scenario 3	Subset 1	59.03	0.00	12.50	0.00	1.39	0.00	2.08	2.78	0.00	1.39	16.67	4.17
	Subset 2	42.71	1.39	13.89	0.69	2.08	0.35	3.47	5.90	0.69	4.17	18.40	6.25
	Subset 3	27.22	3.89	14.44	1.67	4.44	1.94	6.94	9.17	3.33	5.83	14.17	6.94
	Subset 4	16.18	6.25	12.22	1.60	6.81	3.40	9.44	9.24	6.53	7.36	12.36	8.61
	Subset 5	11.11	7.78	9.77	3.52	8.24	5.88	9.12	8.98	9.03	8.24	9.81	8.52
Classification scenario 4	Subset 1	63.89	1.39	8.33	0.00	2.08	2.08	1.39	3.47	0.00	1.39	11.11	4.86
	Subset 2	50.00	1.39	11.11	1.04	2.43	1.04	1.74	3.47	3.13	3.13	13.89	7.64
	Subset 3	28.89	3.33	11.67	2.22	4.44	1.81	5.69	7.50	4.86	5.14	14.03	10.42
	Subset 4	16.25	5.97	9.93	3.68	6.46	3.89	7.22	8.19	8.68	7.71	12.15	9.86
	Subset 5	11.06	7.31	9.21	4.72	7.82	6.62	7.92	7.92	9.86	8.56	10.09	8.89
Classification scenario 5	Subset 1	76.39	0.00	6.94	1.39	0.00	0.00	0.00	3.47	0.00	0.00	10.42	1.39
	Subset 2	59.03	0.35	7.99	4.86	0.35	0.00	0.35	8.33	0.00	0.69	14.93	3.13
	Subset 3	30.42	1.53	11.67	5.94	2.08	2.40	8.19	10.81	1.14	1.94	19.83	4.04
	Subset 4	16.39	3.89	12.85	7.57	4.44	0.90	11.32	12.08	4.03	4.38	15.14	7.01
	Subset 5	11.11	7.59	10.19	6.99	7.73	3.61	10.00	10.05	6.57	7.41	11.06	7.69

signals associated with the 15 EEG electrodes comprised within G_{10} is equal to 68.25 ms (*i.e.*, 4.55 ms × 15 electrodes). Moreover, the average ± standard deviation time required to compute the 45 TFFs within subset 3 for the EEG signals at a particular window position computed across the 16 subjects is equal to 118.3 ± 3.62 ms. Finally, the average ± standard deviation time required to classify each feature vector computed across the 16 subjects is equal to 0.23 ± 0.04 ms. In light of this, the average time required to compute the CWD, extract the TFFs, and recognize the class of the imagined object is equal to 186.78 ms, which is less than the duration of the employed sliding window (*i.e.*, 1000 ms). This suggests the feasibility of utilizing our proposed approach to develop real-world BCI systems.

IV. DISCUSSION
In this study, we explored the potential of decoding visually imagined objects using TFFs that are extracted from the CWD computed from the EEG signals. The performance of our proposed approach was evaluated using EEG signals that were recorded for 16 healthy subjects while imagining 56 different objects that are arranged into four categories, as described in Fig. 1. The results presented in section III demonstrate the capability of our proposed CWD-based approach to accurately decode the visually imagined objects comprised in each of the four categories.

A. RESULTS OF THE CBA AND FBA
The results of the CBA, which are presented in section III-A, show that the CA and F_1 values computed for the EEG groups comprising EEG electrodes that cover the frontal pole, frontal, temporal, and parietal regions of the brain, such as G_6, G_9, and G_{10}, are higher than the CA and F_1 values computed for the other EEG groups. Moreover, Table 3 shows that the EEG groups containing EEG electrodes that cover the occipital region in addition to the frontal pole, frontal, temporal, and parietal regions of the brain, such as G_9 and G_{10}, achieved CA and F_1 values that are higher than the other EEG groups. In addition, the increase in the classification performance obtained for G_7 and G_{10} in comparison with the classification performance obtained for G_5 and G_9, respectively, suggests that the presence of the central region can slightly increase the classification performance. This can be attributed to the influence of the volume conductor on the EEG signals [75], in which the electrical potentials generated within a particular region of the brain are spatially disseminated to other regions and recorded by the sparsely distributed electrodes on the scalp [5], [75].

It is worth to mention that the results of the CBA, which are presented in section III-A, are compliant with the findings reported in previous studies related to visual imagery [37], [76] which have shown that the frontal pole, frontal, temporal, parietal and occipital regions are highly active during the performance of visual imagery task. This in turn justifies the high CA values achieved for each classification scenario using G_{10} compared with the CA values obtained using the other EEG groups which cover subsets of the brain regions in G_{10}. Specifically, Table 3 shows that the highest CA and F_1 values computed for each of the five classification scenarios were archived using G_{10}, which consists of 15 EEG electrodes that cover the central, frontal pole, frontal, temporal, parietal, and occipital regions of the brain.

The results of the FBA, which are provided in Table 4, indicate that using a subset of the TFFs extracted from the EEG electrodes in G_{10} can substantially enhance the classification performance obtained for each classification scenario compared with the classification performance obtained using all the TFFs extracted from the EEG electrodes in G_{10}, which are presented in Table 3. In particular, Table 3 and Table 4 show that the *CA* values obtained for each classification scenario using subset 3, which consists of the highest-ranking 25% of the TFFs extracted from the EEG electrodes in G_{10}, are higher than the *CA* values obtained for each classification scenario using all the TFFs extracted from the EEG electrodes in G_{10}. This can be attributed to the fact that several TFFs that are extracted from different EEG electrodes may comprise redundant and unrelated information [8]. This in turn can increase the similarity between the feature vectors that are extracted from the EEG signals associated with various visually imagined objects, which can degrade the classification performance. Moreover, the *CA* values presented in Fig. 4, which were obtained using the third subset of feature vectors, show a variation in the computed *CA* values among different subjects for the same classification scenario. In fact, this variation in the performance achieved by different subjects is widely known in the literature and commonly referred to as "BCI literacy" [77], [78]. Such a variation can be attributed to the fact that different subjects have different capabilities of performing various mental imagery tasks [18], [53], [61].

B. COMPARISON WITH OTHER EXISTING APPROACHES

Literature reveals that the visual imagery of objects has been mainly investigated using two neuroimaging modalities [28], [33]–[39], namely fMRI and PET. Several limitations, such as the high acquisition cost, low portability, and the requirement of the subject to sit or lay down in the scanner, might limit the wide use of these neuroimaging modalities in visual imagery research labs. Recently, several studies have demonstrated the possibility of decoding visually imagined objects using the EEG neuroimaging modality. For example, Bovrov *et al.* [40] recorded the EEG signals using two different EEG acquisition systems, namely the Emotiv (14 electrodes) and ActiCap (32 electrodes) systems, for seven healthy subjects while imagining two types of objects, namely faces and houses. For each subject, the acquired EEG signals were used to construct a Bayesian classifier to decode the type of the imagined object. The average CA values computed across all subjects based on using the Emotiv and ActiCap EEG acquisition systems were 48% and 54%, respectively. In another study, Esfahani and Sundararajan [12] acquired the EEG signals using the Emotiv EEG acquisition system (14 electrodes) for ten healthy subjects while imagining the shape of five geometric objects. The recorded EEG signals were analyzed using the independent component analysis (ICA) and Hilbert-Huang transform (HHT) to extract a set of spectra-based features from the EEG signals. For each subject, the extracted features

were used to construct five pair-wise linear discriminant classifiers, where each classifier is associated with one of the five objects. The average CA value computed across all subjects and all objects was 44.6%. Kosmyna *et al.* [2] recorded the EEG signals using the 2g.tec USBAmp EEG acquisition system (36 electrodes) for 26 healthy subjects while imagining two objects: a hammer and a daisy flower. For each subject, the acquired EEG signals were used to construct a spectrally weighted common spatial patterns classifier to decode the imagined object. The average CA value computed across all subjects was 55.9%. In a recent study by Wang *et al.* [41], EEG signals were recorded using the actiCHamp Brain Products EEG acquisition system (17 electrodes) for 14 healthy subjects while observing five lowercase letters, including "a", "e", "i", "o", and "t". For each subject, the phase and power data were extracted from the EEG signals and used to construct a multi-class SVM classier to decode the observed letters. The highest average CA value computed across all subjects and all letters was 46.61%.

The work presented in the current study provides three improvements over the approaches described in [2], [12], [40], [41]. First, our proposed approach used a multi-class SVM classifier to discriminate between the visually imagined objects in each of the five classification scenarios, while the approaches presented in [2], [12], [40] utilize binary SVM classifiers to distinguish between individual pairs of visually imagined objects. In this vein, researchers have indicated that decoding various mental tasks using multi-class classification methods is more difficult that decoding a pair of mental tasks [7]. Moreover, the use of multi-class classification methods to decode visually imagined objects can be exploited to advance the BCI technology by using visual imagery as a control paradigm to increase the control dimensionality of EEG-based BCI systems. Additionally, the use of multi-class classification methods to decode the EEG signals recorded for the subjects while imagining digits and letters can facilitate the design of human-computer interfaces that can assist individuals with severe motor and/or lingual impairments. Second, the *CA* values presented in our study were obtained using 15 EEG electrodes compared with the best *CA* values reported in the studies [2], [40], [41] which were obtained using 32, 36, and 17 electrodes, respectively. This illustrates the effectiveness of the TFFs, which are extracted from the CWD computed for EEG segments, in characterizing object-related information to achieve high *CA* values. Third, to the best of our knowledge, this is the first study that investigates the feasibility of classifying 56 different visually imagined objects. The large number of objects considered in the current study increases the difficulty of designing accurate classifiers compared with the aforementioned approaches which considered the problem of classifying two objects, as described in [2], [40], and five objects, as described in [12], [41]. Therefore, our proposed approach has the potential to increase the control dimensionality of EEG-based BCI systems.

R. Alazrai *et al.*: Time-Frequency Distribution-Based Approach for Decoding Visually Imagined Objects Using EEG Signals

IEEE *Access*

C. LIMITATIONS AND FUTURE WORK

Despite the promising results achieved using our proposed approach in distinguishing between the EEG signals associated with various visually imagined objects, we are planning to investigate several research directions that can enhance the accuracy and applicability of our proposed approach. Particularly, we are planning to explore the following future research directions:

(1) Although the runtime of our proposed approach is less than the time range of the employed sliding window, we believe that there is still a room to improve the runtime of the proposed approach using parallel computing technology, which allows the utilization of our approach in various real-time BCI applications.

(2) Our proposed approach utilizes 12 handcrafted TFFs that are extracted from the CWD computed for the EEG signals. In spite of the promising results achieved using these TFFs, the process of designing salient features that can be used to decode different imagery tasks is considered challenging. Motivated by the recent promising results attained in analyzing physiological signals using deep learning approaches [79], [80], we are planning in the future to explore the use of deep learning methods to learn latent features from the CWD computed for the EEG signals to alleviate the need to manually design the features and to enhance the accuracy of decoding visually imagined objects.

(3) The CWD computed for the EEG signals comprises many values that are equal or close to zero. As a consequence, this increases the dimensionality of the computed CWD-based time-frequency representation of the EEG signals, which in turn can increase the computational time of the proposed approach. Recently, researchers have investigated the possibility of using sparse representation classification (SRC) methods to concisely represent multi-dimensional data, such as the CWD computed for the EEG signals, and extract valuable information from the data [81]. For example, Jin *et al.* [82] proposed a sparse Bayesian extreme learning machine classification method to efficiently decode MI tasks. Motivated by the promising results depicted in [82], [83], we intend to investigate the possibility of employing SRC methods to reduce the complexity of our proposed CWD-based approach and enhance the decoding accuracy of visually imagined objects.

(4) As described in section II-B, the size of the images, which are used as visual stimuli, are varied across the four categories. However, for each group, all images were configured to have the same size, where the selected size ensures that the object in the image appears clearly. As part of our future studies, we plan to investigate the impact of the size of the images used as visual stimuli on the conducted visual imagery experiments and the performance of decoding visually imagined objects.

(5) The EEG dataset employed in the current study comprises four object categories. To further investigate the relationship between the performance of the proposed approach and the number of classes and categories, we plan to acquire a large-scale EEG dataset that comprises more object categories and more objects within each category. In addition, we plan to investigate the potential of using hierarchical classification schemes [5], [6] to identify the category of the object at one level of the classification hierarchy and the class of the object at another level. Such a hierarchical classification scheme can simplify the classification problem and enable accurate classification between a higher number of categories and more objects inside each category.

(6) The groups of EEG channels that are used in the CBA, which are depicted in Table 2, were manually created based on neurophysiologic knowledge. Recently, researchers have investigated methodologies to automatically select the most relevant channels to improve classification performance [84], [85]. Inspired by promising results reported in these studies, we plan in the future to investigate the possibility of applying various channel selection algorithms to eliminate redundant information encapsulated within the EEG channels, reduce the complexity of the extracted TFFs, and improve the accuracy of decoding visually imagined objects.

V. CONCLUSION

This study explored the feasibility of using the visual imagery task as a control paradigm to increase the control's dimensions of EEG-based BCI systems. In particular, we have introduced a new EEG-based approach for decoding visually imagined objects that utilizes the CWD to analyze the EEG signals in the joint time-frequency domain and extract a set of twelve novel TFFs. The extracted TFFs were used to build a subject-specific multi-class SVM classifier to decode visually imagined objects. To validate the performance of the proposed approach, we have recorded a large EEG dataset that comprises a wide range of visually imagined objects. The recorded EEG dataset was employed to conduct two performance evaluation analyses to evaluate the capability of our proposed approach to decode different visually imagined objects. The experimental results presented in the current study demonstrate the capability of our proposed approach to accurately decode visually imagined objects based on EEG signal analysis.

REFERENCES

[1] G. Pfurtscheller, C. Guger, G. Müller, G. Krausz, and C. Neuper, "Brain oscillations control hand orthosis in a tetraplegic," *Neurosci. Lett.*, vol. 292, no. 3, pp. 211–214, Oct. 2000.

[2] N. Kosmyna, J. T. Lindgren, and A. Lécuyer, "Attending to visual stimuli versus performing visual imagery as a control strategy for EEG-based brain-computer interfaces," *Sci. Rep.*, vol. 8, no. 1, pp. 1–14, Dec. 2018.

[3] J. R. Wolpaw, N. Birbaumer, D. J. McFarland, G. Pfurtscheller, and T. M. Vaughan, "Brain–computer interfaces for communication and control," *Clin. Neurophysiol.*, vol. 113, no. 6, pp. 767–791, 2002.

[4] L. F. Nicolas-Alonso and J. Gomez-Gil, "Brain computer interfaces, a review," *Sensors*, vol. 12, no. 2, pp. 1211–1279, 2012.

[5] R. Alazrai, H. Alwanni, Y. Baslan, N. Alnuman, and M. Daoud, "EEG-based brain-computer interface for decoding motor imagery tasks within the same hand using choi-williams time-frequency distribution," *Sensors*, vol. 17, no. 9, p. 1937, Aug. 2017.

[6] R. Alazrai, H. Alwanni, and M. I. Daoud, "EEG-based BCI system for decoding finger movements within the same hand," *Neurosci. Lett.*, vol. 698, pp. 113–120, Apr. 2019.

IEEE Access

R. Alazrai *et al.*: Time-Frequency Distribution-Based Approach for Decoding Visually Imagined Objects Using EEG Signals

[7] K. Liao, R. Xiao, J. Gonzalez, and L. Ding, "Decoding individual finger movements from one hand using human EEG signals," *PLoS ONE*, vol. 9, no. 1, Jan. 2014, Art. no. e85192.

[8] R. Alazrai, R. Homoud, H. Alwanni, and M. Daoud, "EEG-based emotion recognition using quadratic time-frequency distribution," *Sensors*, vol. 18, no. 8, p. 2739, Aug. 2018.

[9] R. Alazrai, M. Momani, H. A. Khudair, and M. I. Daoud, "EEG-based tonic cold pain recognition system using wavelet transform," *Neural Comput. Appl.*, vol. 31, no. 7, pp. 3187–3200, Oct. 2017.

[10] R. Alazrai, S. AL-Rawi, H. Alwanni, and M. I. Daoud, "Tonic cold pain detection using Choi–Williams time-frequency distribution analysis of EEG signals: A feasibility study," *Appl. Sci.*, vol. 9, no. 16, p. 3433, Aug. 2019.

[11] L. J. Hadjileontiadis, "EEG-based tonic cold pain characterization using wavelet higher order spectral features," *IEEE Trans. Biomed. Eng.*, vol. 62, no. 8, pp. 1981–1991, Aug. 2015.

[12] E. T. Esfahani and V. Sundararajan, "Classification of primitive shapes using brain–computer interfaces," *Comput.-Aided Des.*, vol. 44, no. 10, pp. 1011–1019, Oct. 2012.

[13] J. Pearson, T. Naselaris, E. A. Holmes, and S. M. Kosslyn, "Mental imagery: Functional mechanisms and clinical applications," *Trends Cognit. Sci.*, vol. 19, no. 10, pp. 590–602, Oct. 2015.

[14] M. Jeannerod, "Mental imagery in the motor context," *Neuropsychologia*, vol. 33, no. 11, pp. 1419–1432, Nov. 1995.

[15] C. Brunner, M. Naeem, R. Leeb, B. Graimann, and G. Pfurtscheller, "Spatial filtering and selection of optimized components in four class motor imagery EEG data using independent components analysis," *Pattern Recognit. Lett.*, vol. 28, no. 8, pp. 957–964, Jun. 2007.

[16] G. E. Fabiani, D. J. McFarland, J. R. Wolpaw, and G. Pfurtscheller, "Conversion of EEG activity into cursor movement by a brain–computer interface (BCI)," *IEEE Trans. Neural Syst. Rehabil. Eng.*, vol. 12, no. 3, pp. 331–338, Sep. 2004.

[17] A. Kübler, B. Kotchoubey, J. Kaiser, J. R. Wolpaw, and N. Birbaumer, "Brain–computer communication: Unlocking the locked in," *Psychol. Bull.*, vol. 127, no. 3, p. 358, 2001.

[18] Y. R. Tabar and U. Halici, "A novel deep learning approach for classification of EEG motor imagery signals," *J. Neural Eng.*, vol. 14, no. 1, Feb. 2017, Art. no. 016003.

[19] G. Pfurtscheller and C. Neuper, "Motor imagery and direct brain-computer communication," *Proc. IEEE*, vol. 89, no. 7, pp. 1123–1134, Jul. 2001.

[20] V. J. Lawhern, A. J. Solon, N. R. Waytowich, S. M. Gordon, C. P. Hung, and B. J. Lance, "EEGNet: A compact convolutional neural network for EEG-based brain–computer interfaces," *J. Neural Eng.*, vol. 15, no. 5, Oct. 2018, Art. no. 056013.

[21] R. T. Schirrmeister, J. T. Springenberg, L. D. J. Fiederer, M. Glasstetter, K. Eggensperger, M. Tangermann, F. Hutter, W. Burgard, and T. Ball, "Deep learning with convolutional neural networks for EEG decoding and visualization," 2017, *arXiv:1703.05051*. [Online]. Available: http://arxiv.org/abs/1703.05051

[22] H. Dose, J. S. Møller, H. K. Iversen, and S. Puthusserypady, "An end-to-end deep learning approach to MI-EEG signal classification for BCIs," *Expert Syst. Appl.*, vol. 114, pp. 532–542, Dec. 2018.

[23] A. J. Doud, J. P. Lucas, M. T. Pisansky, and B. He, "Continuous three-dimensional control of a virtual helicopter using a motor imagery based brain-computer interface," *PLoS ONE*, vol. 6, no. 10, 2011, Art. no. e26322.

[24] A. S. Royer, A. J. Doud, M. L. Rose, and B. He, "EEG control of a virtual helicopter in 3-Dimensional space using intelligent control strategies," *IEEE Trans. Neural Syst. Rehabil. Eng.*, vol. 18, no. 6, pp. 581–589, Dec. 2010.

[25] K. LaFleur, K. Cassady, A. Doud, K. Shades, E. Rogin, and B. He, "Quadcopter control in three-dimensional space using a noninvasive motor imagery-based brain–computer interface," *J. Neural Eng.*, vol. 10, no. 4, Aug. 2013, Art. no. 046003.

[26] M. Taghizadeh-Sarabi, M. R. Daliri, and K. S. Niksirat, "Decoding objects of basic categories from electroencephalographic signals using wavelet transform and support vector machines," *Brain Topography*, vol. 28, no. 1, pp. 33–46, Jan. 2015.

[27] M. G. Philiastides and P. Sajda, "Temporal characterization of the neural correlates of perceptual decision making in the human brain," *Cerebral Cortex*, vol. 16, no. 4, pp. 509–518, Apr. 2006.

[28] M. Misaki, Y. Kim, P. A. Bandettini, and N. Kriegeskorte, "Comparison of multivariate classifiers and response normalizations for pattern-information fMRI," *NeuroImage*, vol. 53, no. 1, pp. 103–118, Oct. 2010.

[29] I. Simanova, M. van Gerven, R. Oostenveld, and P. Hagoort, "Identifying object categories from event-related EEG: Toward decoding of conceptual representations," *PLoS ONE*, vol. 5, no. 12, Dec. 2010, Art. no. e14465.

[30] N. J. Thomas, "Mental imagery, philosophical issues about," *Encyclopedia Cognit. Sci.*, to be published.

[31] S. M. Kosslyn and D. N. Osherson, *An Invitation to Cognitive Science: Visual Cognition*, vol. 2. Cambridge, MA, USA: MIT Press, 1995.

[32] M. Knauff, J. Kassubek, T. Mulack, and M. W. Greenlee, "Cortical activation evoked by visual mental imagery as measured by fMRI," *Neuroreport*, vol. 11, no. 18, pp. 3957–3962, 2000.

[33] E. Mellet, N. Tzourio, M. Denis, and B. Mazoyer, "A positron emission tomography study of visual and mental spatial exploration," *J. Cognit. Neurosci.*, vol. 7, no. 4, pp. 433–445, Oct. 1995.

[34] D. Pearson, R. De Beni, and C. Cornoldi, "The generation, maintenance, and transformation of visuo-spatial mental images," in *Imagery, language and Visuo-Spatial Thinking*. London, U.K.: Psychology Press, 2012, pp. 17–44.

[35] M. D'Esposito, J. A. Detre, G. K. Aguirre, M. Stallcup, D. C. Alsop, L. J. Tippet, and M. J. Farah, "A functional mri study of mental image generation," *Neuropsychologia*, vol. 35, no. 5, pp. 725–730, 1997.

[36] J. Fulford, F. Milton, D. Salas, A. Smith, A. Simler, C. Winlove, and A. Zeman, "The neural correlates of visual imagery vividness—An fMRI study and literature review," *Cortex*, vol. 105, pp. 26–40, Aug. 2018.

[37] S. D. Slotnick, W. L. Thompson, and S. M. Kosslyn, "Visual memory and visual mental imagery recruit common control and sensory regions of the brain," *Cognit. Neurosci.*, vol. 3, no. 1, pp. 14–20, Mar. 2012.

[38] A. M. Albers, P. Kok, I. Toni, H. C. Dijkerman, and F. P. de Lange, "Shared representations for working memory and mental imagery in early visual cortex," *Current Biol.*, vol. 23, no. 15, pp. 1427–1431, Aug. 2013.

[39] T. Horikawa and Y. Kamitani, "Generic decoding of seen and imagined objects using hierarchical visual features," *Nature Commun.*, vol. 8, no. 1, pp. 1–15, Aug. 2017.

[40] P. Bobrov, A. Frolov, C. Cantor, I. Fedulova, M. Bakhnyan, and A. Zhavoronkov, "Brain-computer interface based on generation of visual images," *PLoS ONE*, vol. 6, no. 6, Jun. 2011, Art. no. e20674.

[41] Y. Wang, P. Wang, and Y. Yu, "Decoding english alphabet letters using EEG phase information," *Frontiers Neurosci.*, vol. 12, p. 62, Feb. 2018.

[42] K. N. Kay, T. Naselaris, R. J. Prenger, and J. L. Gallant, "Identifying natural images from human brain activity," *Nature*, vol. 452, no. 7185, pp. 352–355, Mar. 2008.

[43] K. A. Norman, S. M. Polyn, G. J. Detre, and J. V. Haxby, "Beyond mind-reading: Multi-voxel pattern analysis of fMRI data," *Trends Cognit. Sci.*, vol. 10, no. 9, pp. 424–430, Sep. 2006.

[44] B. Boashash, *Time-Frequency Signal Analysis and Processing: A Comprehensive Reference*. New York, NY, USA: Academic, 2015.

[45] M. B. Brodeur, E. Dionne-Dostie, T. Montreuil, and M. Lepage, "The bank of standardized stimuli (BOSS), a new set of 480 normative photos of objects to be used as visual stimuli in cognitive research," *PLoS ONE*, vol. 5, no. 5, May 2010, Art. no. e10773.

[46] P. E. Roland and B. Gulyás, "Visual memory, visual imagery, and visual recognition of large field patterns by the human brain: Functional anatomy by positron emission tomography," *Cerebral Cortex*, vol. 5, no. 1, pp. 79–93, 1995.

[47] S. M. Kosslyn, G. Ganis, and W. L. Thompson, "Neural foundations of imagery," *Nature Rev. Neurosci.*, vol. 2, no. 9, pp. 635–642, Sep. 2001.

[48] T. Horikawa and Y. Kamitani, "Hierarchical neural representation of dreamed objects revealed by brain decoding with deep neural network features," *Frontiers Comput. Neurosci.*, vol. 11, p. 4, Jan. 2017.

[49] J. Shin, K.-R. Müller, and H.-J. Hwang, "Eyes-closed hybrid brain-computer interface employing frontal brain activation," *PLoS ONE*, vol. 13, no. 5, May 2018, Art. no. e0196359.

[50] M. X. Cohen, *Analyzing Neural Time Series Data: Theory and Practice*. Cambridge, MA, USA: MIT Press, 2014.

[51] G. Gomez-Herrero, W. De Clercq, H. Anwar, O. Kara, K. Egiazarian, S. Van Huffel, and W. Van Paesschen, "Automatic removal of ocular artifacts in the EEG without an EOG reference channel," in *Proc. 7th Nordic Signal Process. Symp. NORSIG*, Jun. 2006, pp. 130–133.

[52] B. Boashash and S. Ouelha, "Automatic signal abnormality detection using time-frequency features and machine learning: A newborn EEG seizure case study," *Knowl.-Based Syst.*, vol. 106, pp. 38–50, Aug. 2016.

[53] R. Alazrai, M. Abuhijleh, H. Alwanni, and M. I. Daoud, "A deep learning framework for decoding motor imagery tasks of the same hand using eeg signals," *IEEE Access*, vol. 7, pp. 109612–109627, 2019.

R. Alazrai *et al.*: Time-Frequency Distribution-Based Approach for Decoding Visually Imagined Objects Using EEG Signals

IEEE *Access*

[54] J. M. O. Toole, "Discrete quadratic time-frequency distributions: Definition, computation, and a newborn electroencephalogram application," Ph.D. dissertation, School Med., Univ. Queensland, Brisbane, QLD, Australia, 2009.

[55] H.-I. Choi and W. J. Williams, "Improved time-frequency representation of multicomponent signals using exponential kernels," *IEEE Trans. Acoust., Speech, Signal Process.*, vol. 37, no. 6, pp. 862–871, Jun. 1989.

[56] P. Castiglioni, *Choi–Williams Distribution*. Hoboken, NJ, USA: Wiley, 2005.

[57] S. L. Hahn, *Hilbert Transforms in Signal Processing*, vol. 2. Norwood, MA, USA: Artech House, 1996.

[58] L. Cohen, "Time-frequency distributions—A review," *Proc. IEEE*, vol. 77, no. 7, pp. 941–981, Jul. 1989.

[59] L. Cohen, *Time-Frequency Analysis*, vol. 778. Englewood Cliffs, NJ, USA: Prentice-Hall PTR, 1995.

[60] A. Swami, J. Mendel, and C. Nikias, "Higher-order spectra analysis (HOSA) toolbox, version 2.0. 3," Mathworks Inc., Natick, MA, USA, Tech. Rep. 3, 2000.

[61] M. Ahn and S. C. Jun, "Performance variation in motor imagery brain–computer interface: A brief review," *J. Neurosci. Methods*, vol. 243, pp. 103–110, Mar. 2015.

[62] V. Vapnik, "The support vector method of function estimation," in *Nonlinear Modeling*. Boston, MA, USA: Springer, 1998, pp. 55–85.

[63] A. Y. Ng and M. I. Jordan, "On discriminative vs. Generative classifiers: A comparison of logistic regression and naive Bayes," in *Proc. Adv. Neural Inf. Process. Syst.*, vol. 2, pp. 841–848, 2002.

[64] H. Qian, Y. Mao, W. Xiang, and Z. Wang, "Recognition of human activities using SVM multi-class classifier," *Pattern Recognit. Lett.*, vol. 31, no. 2, pp. 100–111, Jan. 2010.

[65] M. Tavakolan, Z. Frehlick, X. Yong, and C. Menon, "Classifying three imaginary states of the same upper extremity using time-domain features," *PLoS ONE*, vol. 12, no. 3, Mar. 2017, Art. no. e0174161.

[66] X. Yong and C. Menon, "EEG classification of different imaginary movements within the same limb," *PLoS ONE*, vol. 10, no. 4, Apr. 2015, Art. no. e0121896.

[67] U. H.-G. Kreßel, "Pairwise classification and support vector machines," in *Advances in Kernel Methods*. Cambridge, MA, USA: MIT Press, 1999, pp. 255–268.

[68] C.-W. Hsu and C.-J. Lin, "A comparison of methods for multiclass support vector machines," *IEEE Trans. Neural Netw.*, vol. 13, no. 2, pp. 415–425, Mar. 2002.

[69] C. W. Hsu, C. C. Chang, and C. J. Lin, "A practical guide to support vector classification," Dept. Comput. Sci., Nat. Taiwan Univ., Taipei, Taiwan, Tech. Rep., 2003.

[70] Z. Qiu, B. Z. Allison, J. Jin, Y. Zhang, X. Wang, W. Li, and A. Cichocki, "Optimized motor imagery paradigm based on imagining chinese characters writing movement," *IEEE Trans. Neural Syst. Rehabil. Eng.*, vol. 25, no. 7, pp. 1009–1017, Jul. 2017.

[71] H. Peng, F. Long, and C. Ding, "Feature selection based on mutual information criteria of max-dependency, max-relevance, and min-redundancy," *IEEE Trans. Pattern Anal. Mach. Intell.*, vol. 27, no. 8, pp. 1226–1238, Aug. 2005.

[72] D. M. Powers, "Evaluation: From precision, recall and f-measure to ROC, informedness, markedness and correlation," Bioinfo Publications, Pune, India, Tech. Rep., 2011.

[73] S.-M. Zhou, J. Q. Gan, and F. Sepulveda, "Classifying mental tasks based on features of higher-order statistics from EEG signals in brain–computer interface," *Inf. Sci.*, vol. 178, no. 6, pp. 1629–1640, Mar. 2008.

[74] U. R. Acharya, H. Fujita, V. K. Sudarshan, S. Bhat, and J. E. W. Koh, "Application of entropies for automated diagnosis of epilepsy using EEG signals: A review," *Knowl.-Based Syst.*, vol. 88, pp. 85–96, Nov. 2015.

[75] S. P. van den Broek, F. Reinders, M. Donderwinkel, and M. J. Peters, "Volume conduction effects in EEG and MEG," *Electroencephalogr. Clin. Neurophysiol.*, vol. 106, no. 6, pp. 522–534, Jun. 1998.

[76] G. Ganis, W. L. Thompson, and S. M. Kosslyn, "Brain areas underlying visual mental imagery and visual perception: An fMRI study," *Cognit. Brain Res.*, vol. 20, no. 2, pp. 226–241, Jul. 2004.

[77] B. Blankertz, C. Sannelli, S. Halder, E. M. Hammer, A. Kübler, K.-R. Müller, G. Curio, and T. Dickhaus, "Neurophysiological predictor of SMR-based BCI performance," *NeuroImage*, vol. 51, no. 4, pp. 1303–1309, Jul. 2010.

[78] M. Ahn, H. Cho, S. Ahn, and S. C. Jun, "High theta and low alpha powers May be indicative of BCI-illiteracy in motor imagery," *PLoS ONE*, vol. 8, no. 11, Nov. 2013, Art. no. e80886.

[79] X. Zhang, L. Yao, X. Wang, J. Monaghan, D. Mcalpine, and Y. Zhang, "A survey on deep learning based brain computer interface: Recent advances and new frontiers," 2019, *arXiv:1905.04149*. [Online]. Available: http://arxiv.org/abs/1905.04149

[80] O. Faust, Y. Hagiwara, T. J. Hong, O. S. Lih, and U. R. Acharya, "Deep learning for healthcare applications based on physiological signals: A review," *Comput. Methods Programs Biomed.*, vol. 161, pp. 1–13, Jul. 2018.

[81] J. Wright, A. Y. Yang, A. Ganesh, S. S. Sastry, and Y. Ma, "Robust face recognition via sparse representation," *IEEE Trans. Pattern Anal. Mach. Intell.*, vol. 31, no. 2, pp. 210–227, Feb. 2009.

[82] Z. Jin, G. Zhou, D. Gao, and Y. Zhang, "Eeg classification using sparse Bayesian extreme learning machine for brain–computer interface," *Neural Comput. Appl.*, vol. 32, no. 11, pp. 6601–6609, Jun. 2020.

[83] D. Wen, P. Jia, Q. Lian, Y. Zhou, and C. Lu, "Review of sparse representation-based classification methods on EEG signal processing for epilepsy detection, brain-computer interface and cognitive impairment," *Frontiers Aging Neurosci.*, vol. 8, p. 172, Jul. 2016.

[84] J. Jin, Y. Miao, I. Daly, C. Zuo, D. Hu, and A. Cichocki, "Correlation-based channel selection and regularized feature optimization for MI-based BCI," *Neural Netw.*, vol. 118, pp. 262–270, Oct. 2019.

[85] H. Chang and J. Yang, "Automated selection of a channel subset based on the genetic algorithm in a motor imagery brain-computer interface system," *IEEE Access*, vol. 7, pp. 154180–154191, 2019.

RAMI ALAZRAI (Member, IEEE) received the Ph.D. degree in electrical and computer engineering from Purdue University, West Lafayette, IN, USA, in 2013. In June 2013, he joined the School of Electrical Engineering and Information Technology, German Jordanian University (GJU), where he is currently an Associate Professor. His research interests include machine learning, biomedical imaging and signal processing, brain-computer interfaces, actual decoding and imaginary motor tasks using EEG signals, decoding visually imagined objects, EEG-based emotion identification, EEG-based pain analysis, semantic video analysis, human activity recognition, emotion recognition, human-to-human interaction representation and analysis, and elderly fall detection.

AMAL AL-SAQQAF received the B.S. degree in software engineering from Taiz University, Taiz, Yemen, in 2012. She is currently pursuing the M.S. degree in computer engineering with German Jordanian University, Amman, Jordan. She worked as a Teaching Assistant with the Department of Software Engineering, Taiz University. Her research interests include machine learning, EEG signal processing, and brain-computer interfaces.

FERAS AL-HAWARI received the B.S. degree in electrical and computer engineering from the Jordan University of Science and Technology, Irbid, Jordan, in 1993, the M.S. degree in computer engineering from the Florida Institute of Technology, Melbourne, USA, in 1995, and the Ph.D. degree in electrical engineering from Northeastern University, Boston, USA, in 2007. He was a Senior Member of the Consulting Staff as well as a Technical Lead of the circuit simulation and signal integrity analysis technologies with the Allegro Printed Circuit Board (PCB) SI Research and Development Group. He is currently an Associate Professor of computer engineering, and the Director of the Information Systems and Technology Center, German Jordanian University. He is the Founder of the Software Development Division at the center. Previously, he worked with Cadence Design Systems Inc., Chelmsford, USA, from 1995 to 2012. He holds seven USA patents and several other publications. His research interests include software engineering, application security, ERP tools development, signal integrity, PCB design, circuit simulation, the IoT, and big data. He is an Associate Editor of the IEEE TRANSACTIONS ON COMPONENTS, PACKAGING, AND MANUFACTURING TECHNOLOGY (TCPMT).

HISHAM ALWANNI received the B.S. degree in mechatronics engineering from German Jordanian University, Amman, Jordan, in 2016. He is currently pursuing the master's degree with the Faculty of Engineering, University of Freiburg, Germany. His research interests include EEG signal processing, brain-computer interfaces, deep learning in medical image analysis, and virtual reality.

MOHAMMAD I. DAOUD received the Ph.D. degree in electrical and computer engineering from the University of Western Ontario, London, Canada, in 2009. During the graduate studies, he was awarded the NSERC PGS-D Scholarship and served as a Scholar of the Canadian Institutes of Health Research/University of Western Ontario Strategic Training Initiative in Cancer Research and Technology Transfer. After finishing the graduate studies, he worked with the Department of Electrical and Computer Engineering, The University of British Columbia, Vancouver, Canada, as a Postdoctoral Research Fellow, where he held an NSERC Postdoctoral Fellowship. In September 2011, he joined the Department of Computer Engineering, German Jordanian University, Amman, Jordan, where he is currently an Associate Professor. His research interests include medical image and signal processing, 3D ultrasound imaging, image-guided surgery, computer-aided diagnosis systems, machine learning, deep learning, and parallel computing.

● ● ●